















Tidal Distortions in NGC1052-DF2 and NGC1052-DF4: Independent Evidence for a Lack of Dark Matter

MICHAEL A. KEIM ¹, PIETER VAN DOKKUM ¹, SHANY DANIELI ^{2,3,*}, DEBORAH LOKHORST ^{4,5},
JIAXUAN LI (李嘉轩) ², ZILI SHEN ¹, ROBERTO ABRAHAM ^{4,5}, SEERY CHEN ^{4,5}, COLLEEN GILHULY ^{4,5},
QING LIU (刘青) ^{4,5}, ALLISON MERRITT ⁶, TIM B. MILLER ¹, IMAD PASHA ¹ AND AVA POLZIN ¹

¹*Department of Astronomy, Yale University, PO Box 208101, New Haven, CT 06520-8101, USA*

²*Department of Astrophysical Sciences, 4 Ivy Lane, Princeton University, Princeton, NJ 08544*

³*Institute for Advanced Study, 1 Einstein Drive, Princeton, NJ 08540, USA*

⁴*Department of Astronomy & Astrophysics, University of Toronto, 50 St. George St., Toronto, ON M5S 3H4, Canada*

⁵*Dunlap Institute for Astronomy and Astrophysics, University of Toronto, Toronto ON, M5S 3H4, Canada*

⁶*Max-Planck-Institut für Astronomie, Königstuhl 17, D-69117 Heidelberg, Germany*

ABSTRACT

Two ultra diffuse galaxies in the same group, NGC1052-DF2 and NGC1052-DF4, have been found to have little or no dark matter and to host unusually luminous globular cluster populations. Such low mass diffuse objects in a group environment are easily disrupted and are expected to show evidence of tidal distortions. In this work we present deep new imaging of the NGC1052 group obtained with the Dragonfly Telephoto Array to test this hypothesis. We find that both galaxies show strong position angle twists and are significantly more elongated in their outskirts than in their interiors. The group's central massive elliptical NGC1052 is the most likely source of these tidal disturbances. The observed distortions imply that the galaxies have a very low total mass; otherwise, they must be very close to NGC1052. Taking into account a recently derived lower limit on the relative line-of-sight distance between NGC1052-DF2 and NGC1052-DF4 from the tip of the red giant branch stars, we infer that the dark matter halo masses of these galaxies cannot be much greater than their stellar masses. Our findings provide strong evidence, completely independent of kinematic constraints, that both galaxies are indeed dark matter deficient. While tidal distortions do not directly provide new information on the formation of NGC1052-DF2 and NGC1052-DF4, the similarity of their tidal features suggests that they are at comparable distances from NGC1052.

Keywords: Dark matter (353) — Galaxy evolution (594) — Galaxy structure (622) — Low surface brightness galaxies (940) — Tidal distortion (1697)

1. INTRODUCTION

The galaxies NGC1052-DF2 and NGC1052-DF4 both have little to no dark matter based on the velocity dispersion of kinetic tracers (van Dokkum et al. 2018a; Wasserman et al. 2018; van Dokkum et al. 2019; Danieli et al. 2019; Emsellem et al. 2019) and host a unique population of globular clusters nearly two magnitudes brighter than expected (van Dokkum et al. 2018b; Ma et al. 2020; Shen et al. 2021a). They are likely associated

with the massive elliptical NGC1052 (Shen et al. 2021b) and fall into the category of ultra diffuse galaxies; large, faint objects with the sizes of L_* galaxies but the stellar masses of dwarf galaxies (van Dokkum et al. 2015).

Both their luminous globular clusters and low dark matter content set NGC1052-DF2 and NGC1052-DF4 apart from almost all other galaxies known. The near-universal globular cluster luminosity function has a peak at $M_V \approx -7.5$ mag (Rejkuba 2012), whereas the NGC1052-DF2 and NGC1052-DF4 distributions peak at $M_V \approx -9$ mag (Shen et al. 2021a). Galaxies with the stellar mass of NGC1052-DF2 and NGC1052-DF4 (approximately $2.0 \times 10^8 M_\odot$ and $1.5 \times 10^8 M_\odot$, respectively; van Dokkum et al. 2018a, 2019) ought to have a >300

Corresponding author: Michael A. Keim
michael.keim@yale.edu

* NASA Hubble Fellow

times more massive dark matter halo (Behroozi et al. 2013). However, their inferred total masses are of the same order as their stellar masses alone.

The observation of two independent galaxies each displaying the same remarkable properties suggests the low dark matter content is not the consequence of mass measurement uncertainties. Yet, an important question remains regarding the apparent lack of tidal distortions in the Dragonfly Telephoto Array (Dragonfly; Abraham & van Dokkum 2014) images which first identified NGC1052-DF4 and brought renewed interest in NGC1052-DF2 (van Dokkum et al. 2018a, 2019). A kpc-scale object with a dwarf galaxy’s stellar content and no dark matter is fragile, and material on its outskirts should be easily unbound by the gravitational pull of other galaxies in a group environment. However, both galaxies have a smooth, spheroidal morphology in the initial Dragonfly images. At face value this does not support the conclusion that the galaxies are dark matter deficient.

One possible explanation for the inconsistency is that the galaxies are in the outskirts of the group, far from the central galaxy. Indeed, the recently measured line-of-sight distance between NGC1052-DF2 and NGC1052-DF4 of 2.1 ± 0.5 Mpc (Shen et al. 2021b) implies that at least one of the galaxies may be at a considerable distance from the center of the NGC1052 group. Their similar, extraordinary properties suggests that the two galaxies formed through the same mechanism, so it is unlikely the galaxies are so close on the sky by chance. However, it is possible one or both of the galaxies was ejected from the NGC1052 group in the distant past, such that ongoing interactions are weak and distortions from previous interactions have dissipated. This may be in line with proposed formation scenarios that include high velocity collisions (see, e.g., Silk 2019 and Shin et al. 2020) or backsplash orbits (Benavides et al. 2021).

A second explanation of the apparent lack of tidal features is that the initial Dragonfly images’ depth, a 1σ surface brightness limit of $\mu_g \sim 29$ mag arcsec $^{-2}$ on $12''$ scales (van Dokkum et al. 2018a), was insufficient to detect them. Recent studies have obtained deeper imaging and have indeed found evidence for distortions. Montes et al. (2020) find that NGC1052-DF4 becomes disrupted at $\sim 44''$, where the galaxy’s profile reaches a surface brightness of $\mu_g \sim 29$ mag arcsec $^{-2}$. Similarly, NGC1052-DF2 appears to be elongated at large radii in Fig. 3 of Müller et al. (2019). However, a recent analysis by Montes et al. (2021) does not interpret NGC1052-DF2 as being tidally distorted.

In this work we return to Dragonfly to explore tidal features associated with the dark matter deficient galaxies, producing the deepest image yet taken by the array. We start with a brief discussion of the utility of tidal structures to probe a galaxy’s mass and orbit in Section 2. In Section 3, we outline our observations and the data reduction procedures we use to isolate low surface brightness emission. In Section 4 we describe and analyze our images of NGC1052-DF2 and NGC1052-DF4 and use their derived morphology to constrain their masses and orbits. We place our work in a wider context in Section 5, and give a final summary of our findings in Section 6. Where relevant, we assume a flat, Lambda Cold Dark Matter (Λ CDM) cosmological model with a Hubble constant $H_0 = 67.4$ km s $^{-1}$ Mpc $^{-1}$ and density parameters $\Omega_M = 0.315$ and $\Omega_\Lambda = 0.685$ (Planck Collaboration et al. 2020).

2. TIDAL DISTORTIONS

Satellite galaxies in a group environment are tidally disturbed by the gravitational pull of other galaxies in the group. At a point known as the tidal radius, material in the satellite becomes unbound by the perturbing galaxy and is stripped away. If we consider two galaxies orbiting at a distance R and account for a centrifugal force, the radius r_{tid} where the tidal force from a perturber M is greater than the self gravity of a satellite m is given by

$$r_{\text{tid}} = R \times \left(\frac{m(r_{\text{tid}})/M(R)}{2 + \frac{\Omega^2 R^3}{GM(R)} - \frac{d \ln M}{d \ln R} \bigg|_R} \right)^{1/3} \quad (1)$$

where $m(r)$ and $M(R)$ are the satellite and perturber’s mass profiles, respectively, and $\Omega = |\vec{V} \times \vec{R}|/R^2$ is the angular speed of the satellite (King 1962; Mo et al. 2010). Note that other definitions of the tidal radius exist in literature, as reviewed by van den Bosch et al. (2018), with Eq. (1) making the least assumptions. In the limit that the galaxies are on a circular orbit sufficiently large so that $m(r)$ and $M(R)$ may be treated as point masses, Eq. (1) reduces to

$$r_J = R \times \left(\frac{m}{3M} \right)^{1/3}, \quad (2)$$

i.e., the classical Jacobi radius (Binney & Tremaine 2008).

In Fig. 1, we demonstrate how the tidal radius of a satellite galaxy moving through the potential of NGC1052 (as taken from Forbes et al. 2019) depends on the satellite’s orbital distance, orbital velocity, total

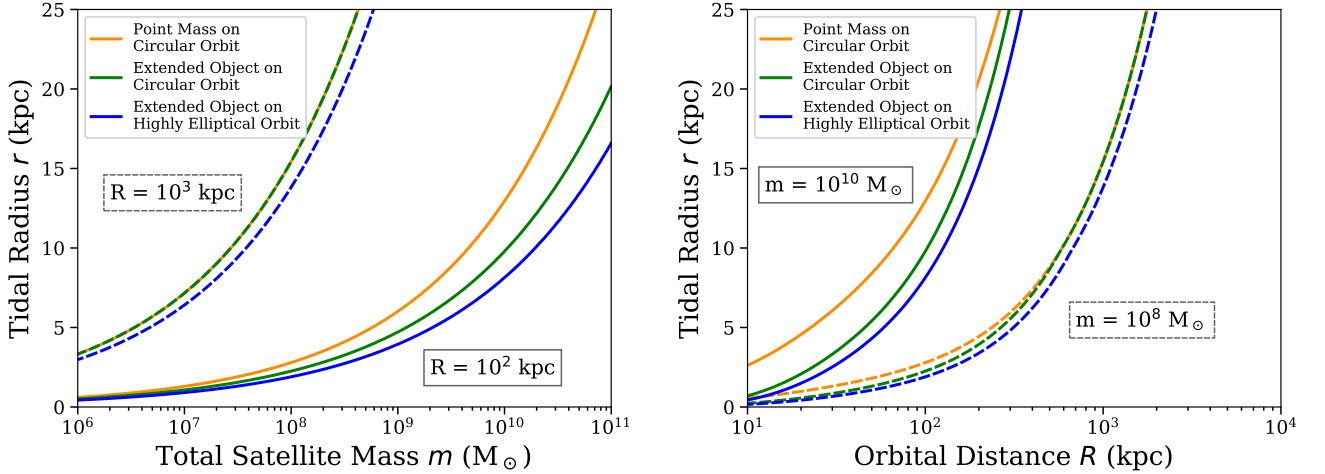


Figure 1. A demonstration of how the tidal radius depends on properties of the satellite and its orbit using Eq. (1). Material in the satellite beyond the indicated tidal radius will be stripped by NGC1052. *Left panel:* The tidal radius as a function of total satellite mass m at two different distances from NGC1052, 10^2 and 10^3 kpc. *Right panel:* The tidal radius as a function of orbital distance R for two different satellite masses, 10^8 and $10^{10} M_\odot$. We first show r_{tid} for a point mass on a circular orbit (orange lines), then compare to an extended satellite with a Navarro-Frenk-White (NFW; Navarro et al. 1997) profile using a concentration $c = 9.6 \times (m/10^{13} M_\odot)^{-0.13} \times (1+z)^{-1}$ (Bullock & Johnston 2005) and a virial radius $r_{\text{vir}} = (Gm/100H^2(z))^{1/3}$ (green lines). Finally, we include the same extended satellite on a highly elliptical orbit with an angular speed $\Omega = \sqrt{2}V_{\text{circ}}/R$, i.e. the maximum possible tidal radius for a bound orbit (blue lines). NGC1052’s mass profile $M(R)$ is taken from Forbes et al. (2019), an NFW profile with $c = 7.0$, $M_{\text{vir}} = 6.2 \times 10^{12} M_\odot$, $R_{\text{vir}} = 390$ kpc, untruncated to account for other objects within the group, and a $4 \times 10^{11} M_\odot$ central baryonic component.

mass, and mass distribution.¹ The group’s central elliptical NGC1052 represents the most likely perturber due to its high mass and relative proximity to NGC1052-DF2 and NGC1052-DF4 (Blakeslee et al. 2001; Danieli et al. 2020; Shen et al. 2021b).²

Fig. 1 shows that less massive satellites are more fragile and will be tidally stripped at smaller radii. A low mass satellite must be orbiting at a much larger distance to have the same tidal radius as a more massive satellite. This effect is amplified if we consider an object’s spatial extent, since material throughout the satellite will have a lower self gravity, experiencing the inward pull of less enclosed mass at greater distances. It is also amplified if we consider angular speeds exceeding that of a circular orbit, as this leads to a greater inward acceleration toward the perturber making it easier for mate-

rial to be gravitationally unbound. Since the dark matter deficient, ultra diffuse galaxies NGC1052-DF2 and NGC1052-DF4 each have an especially low mass and large spatial extent, they are easily tidally disrupted. This is an important consequence, though not necessarily the cause, of the galaxies’ dark matter deficiency.

One clear observational signature of the tidal radius are S-shaped tidal tails which indicate stellar material actively being stripped away from the satellite by a perturbing galaxy (McConnachie & Irwin 2006; Koch et al. 2012; Mowla et al. 2017). If one does not observe tidal tails, this may imply that the tidal radius has not been directly observed. However, internal morphological distortions related to tidal interactions may be observed even without the detection of tidal tails. Such features may be identified through the stretching or twisting of isophotes (Johnston et al. 2002; De Rijcke et al. 2006; Battaglia et al. 2012; Mowla et al. 2017), although in this case inferring the precise location of the tidal radius becomes more complicated. These distortions may represent bound material within the tidal radius being heated by an ongoing interaction, or they may be tidal relics – remnants of an interaction that occurred in the past, for instance at the pericentric passage of an elliptical orbit where tidal interactions are strongest. Indeed, a number of works have made the approximation that

¹ Note that here we only consider the satellite’s halo to present a generalized case, since dark matter dominates the total mass and outer density profile of most galaxies. However, this is not appropriate for dark matter deficient galaxies. Thus, in Section 4 we also consider a fixed stellar component based on the observed Sérsic profile.

² We will show later that the morphologies of the galaxies are consistent with this assumption. The galaxies have very similar tidal distortions, even though they are not close to each other on the sky. This similarity, shown in Section 4, implies they are experiencing a similar tidal field – as expected when NGC1052 is the perturber.

the onset of observed distortions is equal to the tidal radius at pericenter (e.g. Faber 1973; Choi et al. 2002).

Numerical simulations present an opportunity to move beyond this approximation and to consider the cumulative effects of the instantaneous tidal radius throughout a satellite’s orbit, rather than just at pericentric passage. For instance, Johnston et al. (2002) modeled the destruction of satellites in various orbits and compared the actual tidal radius to what one would infer from elliptical isophotes over hundreds of snapshots and a range of viewing angles. They found that the onset of morphological distortions and breaks in a satellite’s surface brightness profile at r_{distort} and r_{break} , respectively, could be observed a factor of a few inwards of the true instantaneous tidal radius. Throughout all considered orbits

$$r_{\text{distort}} \lesssim r_{\text{tid,inst}} \lesssim 2 \times r_{\text{break}}, \quad (3)$$

where Johnston et al. (2002)’s instantaneous tidal radius $r_{\text{tid,inst}}$ is calculated assuming a circular orbit but considering the mass profiles of each galaxy; i.e., Eq. (2) replacing m with $m(r_{\text{tid,inst}})$ and M with $M(R)$. In this case, Fig. 1 indicates that even if the dark matter deficient galaxies are $\gtrsim 1$ Mpc away from NGC1052, we might still be able to observe the tidal disruption of gravitationally bound material.

The relations from Johnston et al. (2002) are a useful tool to characterize a galaxy’s mass and orbit, and should theoretically still be accurate whether or not tidal features primarily arose at pericentric passage since the authors analyzed what would be inferred from observation at well sampled orbital locations. Even so, we caution readers that it is possible NGC1052-DF2 and NGC1052-DF4’s trajectories may not be well described by any of the models presented, which only considered orbits with pericenters at 30 kpc and apocenters at 37, 55, 150, and 450 kpc. Moreover, the concept of tidal radii in general has flaws that have been extensively reviewed in the literature (e.g. Taylor & Babul 2001; Zentner & Bullock 2003; Read et al. 2006; Binney & Tremaine 2008; Mo et al. 2010; van den Bosch et al. 2018), breaking down in specific regimes where underlying approximations are invalid (e.g. $r_{\text{tid}} \sim R$) and being generally incorrect in assuming a perfectly spheroidal surface where material is unbound. Finally, we note that isophote twists may also result from the projection of a triaxial system with radially-varying axis ratios rather than tidal disruption, although the resulting position angle changes tend to be small (van Dokkum & Franx 1995).

3. DATA

3.1. Observations and Reduction

Images of the NGC1052 field were obtained with the 48-lens Dragonfly Telephoto Array (Abraham & van Dokkum 2014; Danieli et al. 2020). Each of the 48 Canon 400 mm f/2.8 II telephoto lenses that are in the array is outfitted with a Santa Barbara Imaging Group (SBIG) CCD camera, with an instantaneous field of view of 2.6×1.9 and a pixel scale of $2''.85 \text{ pixel}^{-1}$. Redundancy is achieved by offsetting the lenses from one another by $\approx 10\%$ of the field of view and by large dithers between individual exposures. Individual observing sequences consisted of nine exposures of 600 s each, dithered in a quasi-random pattern in a $45'$ box. Owing to the dithering, the final image covers 12 deg^2 , with reduced depth near the edges of the field. Images were taken in both g and r bands simultaneously with half (24) of the lenses equipped with Sloan- g filters and half with Sloan- r . The observations took place during 18 nights between October 2018 and February 2019.

The data reduction was performed using the customized Dragonfly Reduction Pipeline software, described in detail in Danieli et al. (2020) and in Zhang (2018). Briefly, a set of algorithms assesses the quality of individual frames, retaining only high-quality data. The sky modeling and subtraction is performed in two stages, ensuring that low surface brightness features with spatial scales up to 0.9×0.6 are preserved. All the data processing steps were performed using batch processing protocols on the Canadian Advanced Network for Astronomical Research (CANFAR) cloud. The final g and r -band co-added images consist of 2346 and 2603 frames respectively. This is equivalent to 17.2 hrs with the full 48-lens array (8.14 hrs in g -band and 9.04 hrs in r -band).

In addition to our new Dragonfly observation, this work also makes use of Dark Energy Camera (DECam) Legacy Survey (DECaLS; Dey et al. 2019) data to model high surface brightness objects (see Section 3.2) as well as deep *Hubble Space Telescope* (*HST*) Advanced Camera for Surveys (ACS) imaging to study the morphology of the galaxies’ inner regions (see Section 4.3). DECaLS g - and r -band data was accessed from Data Release 8 (DR8). *HST* observations, as detailed in Danieli et al. (2020) and Shen et al. (2021b), were taken during Cycles 24 (program 14644), 26 (program 15695), and 27 (program 15851), imaging NGC1052-DF4 over 8 orbits in the F814W filter and 4 orbits in the F606W filter and NGC1052-DF2 over 20 orbits in each filter.

Fig. 2 presents a composite view of the data utilized in our study, with low surface brightness emission from Dragonfly given in black and white, high surface brightness objects from DECaLS displayed in color (Lupton et al. 2004), and a zoomed-in view of the two dark matter deficient galaxies from *HST* shown in inset panels.

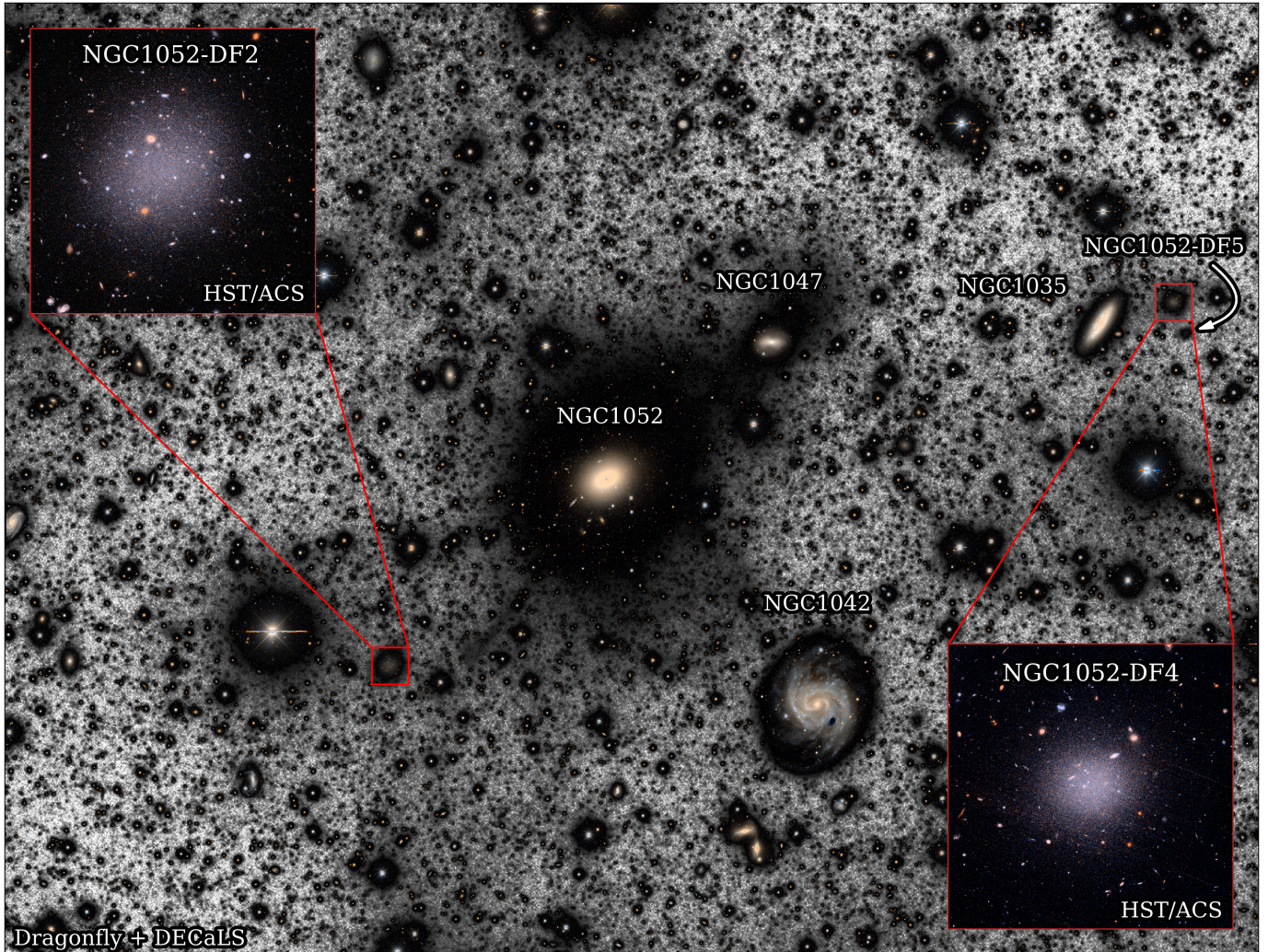


Figure 2. The NGC1052 field. A composite $g + r$ Dragonfly image (*greyscale*) covers the central 1.0×0.75 deg region cutout from the original 12 deg^2 field. High surface brightness objects in the same region are displayed using data from DECaLS (*multi-color*). The $1.75' \times 1.75'$ areas surrounding NGC1052-DF2 and NGC1052-DF4 are shown using deep *HST* images from Shen et al. (2021b) and Danieli et al. (2020) observed with the ACS over 40 and 12 orbits, respectively (*zoom-in panels*).

The field is a beautiful collection of spiral, elliptical, and dwarf galaxies. Such a dense group has a strong gravitational effect on its satellites, and as a result in Fig. 2 we see evidence of interaction between NGC1052 and both NGC1042 and NGC1047.

3.2. Multi-resolution Filtering

The presence of compact, high surface brightness sources like foreground stars, globular clusters, and galaxies complicates our search for low surface brightness tidal features, obscuring tidal tails and hindering fits to the ultra diffuse galaxies' emission. Thus, before continuing our analysis we must remove high surface brightness emission. However, while Dragonfly's sensitivity is optimal for imaging low surface brightness structures, its spatial resolution – a PSF FWHM of $5''$ – is not sufficient to resolve many compact sources. This

may lead to the misidentification of groups of stars and galaxies as low surface brightness emission. We therefore adopt the multi-resolution filtering (MRF) procedure of van Dokkum et al. (2020), using higher resolution DECaLS data to create a model of high surface brightness emission which is then matched to Dragonfly's resolution and subtracted. A visualization of key MRF steps as they are applied to NGC1052-DF2 and NGC1052-DF4 is given in Fig. 3. The remainder of this section summarizes our application of this procedure.

First, to mitigate sampling effects we bin DECaLS g - and r -band images into 2×2 pixel regions and convolve with a $\sigma = 1$ pixel Gaussian. To account for differences in the instrumental response between the DECam and

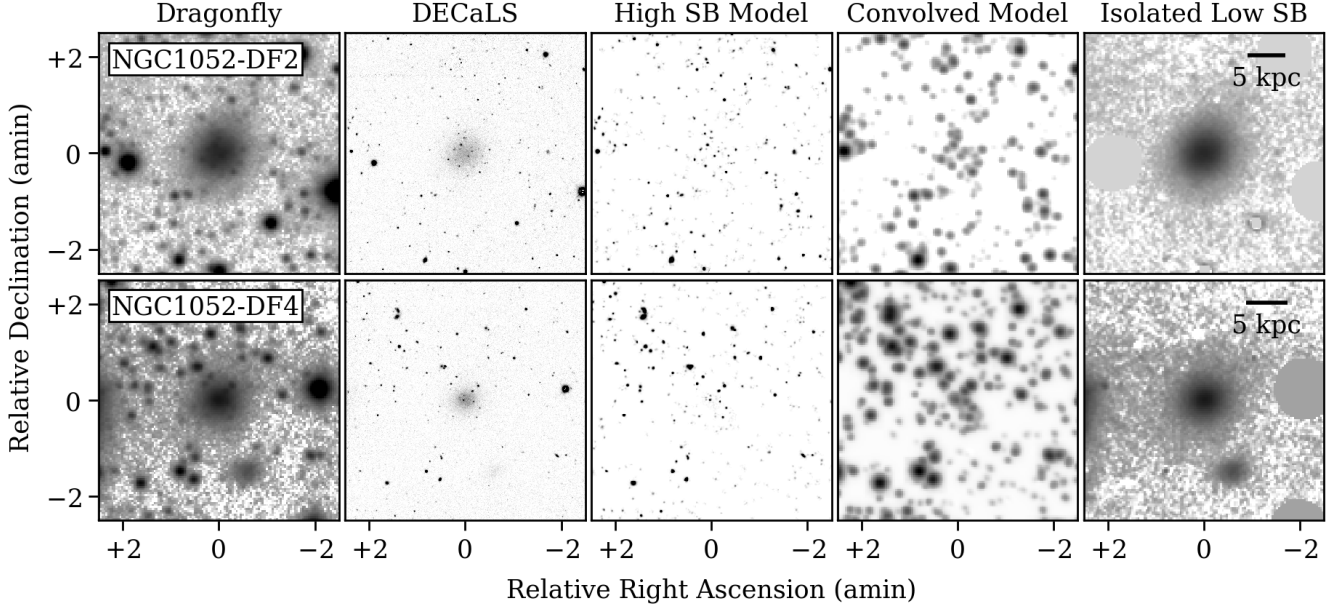


Figure 3. A visualization of MRF as we apply it to the NGC1052 field in the r -band for NGC1052-DF2 (top) and NGC1052-DF4 (bottom). *Left panel:* The initial Dragonfly image with both high and low surface brightness emission. *Second panel:* The initial, higher resolution DECaLS image. *Third panel:* A flux model of compact objects detected in the high resolution image. *Fourth panel:* The same flux model convolved with a characteristic kernel derived from bright stars in order to match Dragonfly resolution. *Right panel:* The final, masked residual Dragonfly image after subtracting the convolved flux model. We adopt normalizations that best display the MRF technique. Right ascension and declination are given relative to $\alpha_{\text{DF2}} = 02^{\text{h}}41^{\text{m}}46^{\text{s}}.8$, $\delta_{\text{DF2}} = -08^{\circ}24'09''.7$ and $\alpha_{\text{DF4}} = 02^{\text{h}}39^{\text{m}}15^{\text{s}}.1$, $\delta_{\text{DF4}} = -08^{\circ}06'57''.6$ and scale bars are based on distances from [Danieli et al. \(2020\)](#) and [Shen et al. \(2021b\)](#).

Dragonfly filter systems we apply a color correction

$$I_{\nu_{\text{DF}}}(\alpha, \delta) = I_{\nu_{\text{DCLS}}}(\alpha, \delta) \times \left(\frac{I_{g_{\text{DCLS}}}(\alpha, \delta)}{I_{r_{\text{DCLS}}}(\alpha, \delta)} \right)^{\gamma(\nu)}, \quad (4)$$

that is, the ν_{DCLS} band at a right ascension α and declination δ is multiplied by the ratio of DECaLS g - to r -band flux raised to a filter-dependent power of either $\gamma(g) = 0.05$ or $\gamma(r) = 0.01$. Pixels with unusually high or low color ratios (artifacts or objects with steep spectra) are subtracted.

Next, we generate a high surface brightness flux model by identifying compact sources in the DECaLS data with [Barbary \(2016\)](#)'s implementation of Source Extractor ([Bertin & Arnouts 1996](#)) and removing undesired objects. This includes low surface brightness emission with $\mu > 25.5 \text{ mag arcsec}^{-2}$, which we do not want to subtract from the Dragonfly data, and stars brighter than a magnitude of 17. Such bright stars are saturated in the high resolution image leading to inaccurate flux values in the model, and their emission may have a large spatial extent, complicating our convolution used to match Dragonfly's resolution.

We then create the kernel that is needed to convolve the flux model to Dragonfly's resolution. This is done by identifying isolated, non-saturated bright

stars and taking the ratio of the Fourier transform of the low resolution image to the high resolution image. We select the median kernel generated from 24 stars, the brightest stars under an upper limit (a fraction $f_r = 1.5\%$, $f_g = 10\%$ of the brightest 10 objects) and sufficiently circular to eliminate galaxies (an axis ratio of $b/a = 0.7$). We convolve our flux model with the median kernel to get an image that matches Dragonfly's resolution. We then subtract this, along with a constant sky background, from the Dragonfly image. Remaining bright stars are subtracted and artifacts brighter than a magnitude of 16 are masked. After completion, we found that slightly too much flux remained in the high surface brightness model such that the subtraction left shallow cavities in NGC1052-DF2, NGC1052-DF4, and NGC1052-DF5. We therefore subtracted an initial model of emission from these three galaxies in the DECaLS image before running MRF, to ensure no emission from the low surface brightness galaxies remained in the high surface brightness map. We generated these models by subtracting the sky background and compact sources identified by Source Extractor using an aggressive background removal (`BACK_SIZE = 8`), and modeling the remaining structure using Photutils ([Bradley et al. 2020](#)'s Python implementation of the isophote fitting algorithm

of Jedrzejewski 1987). A description of this method as applied to Dragonfly data is given in Section 4.1.

3.3. Limiting Depth

Quantifying the surface brightness limit for images of extended sources is a non-trivial task, and the specific methodologies used as well as the presence of large scale gradients in the image significantly impacts the estimated depth. In this work, we measure the surface brightness limit as the contrast on particular spatial scales using the method of van Dokkum et al.³ which estimates variation across binned, background subtracted fluxes. With optimized masks, we find a 1σ limit of $\mu_g = 31.29 \text{ mag arcsec}^{-2}$ on $60''$ scales, a 1σ limit of $\mu_g = 30.24 \text{ mag arcsec}^{-2}$ on $12''$ scales, and a 3σ limit of $\mu_g = 28.90 \text{ mag arcsec}^{-2}$ on $10''$ scales. Note that if we instead utilize the method described in Appendix A of Román et al. (2020), fitting a Gaussian to the Poisson noise of the data, we arrive at a 1σ limit of $\mu_g = 32.49 \text{ mag arcsec}^{-2}$ at $60''$ scales, a 1σ limit of $\mu_g = 30.74 \text{ mag arcsec}^{-2}$ at $12''$ scales, and a 3σ limit of $\mu_g = 29.35 \text{ mag arcsec}^{-2}$ at $10''$ scales.⁴

4. RESULTS

4.1. Image Analysis

In Fig. 4 we present the surface brightness map of both dark matter deficient galaxies after applying MRF, averaging the g and r photometric bands to increase the signal-to-noise (S/N) ratio. We also apply a local background correction, subtracting the mean flux of the regions listed in Appendix A. While the inner contours of NGC1052-DF2 and NGC1052-DF4 are round as in van Dokkum et al. (2018a, 2019), the outer contours of both galaxies appear to become elliptical. This morphology is in agreement with the results of Müller et al. (2019, see Fig. 3) and Montes et al. (2020).

In the case of NGC1052-DF4, our morphological analysis is impeded by the presence of NGC1052-DF5 and NGC1035, whose light overlaps with NGC1052-DF4 in sky projection. Thus, in order to better understand NGC1052-DF4's outskirts and investigate the presence

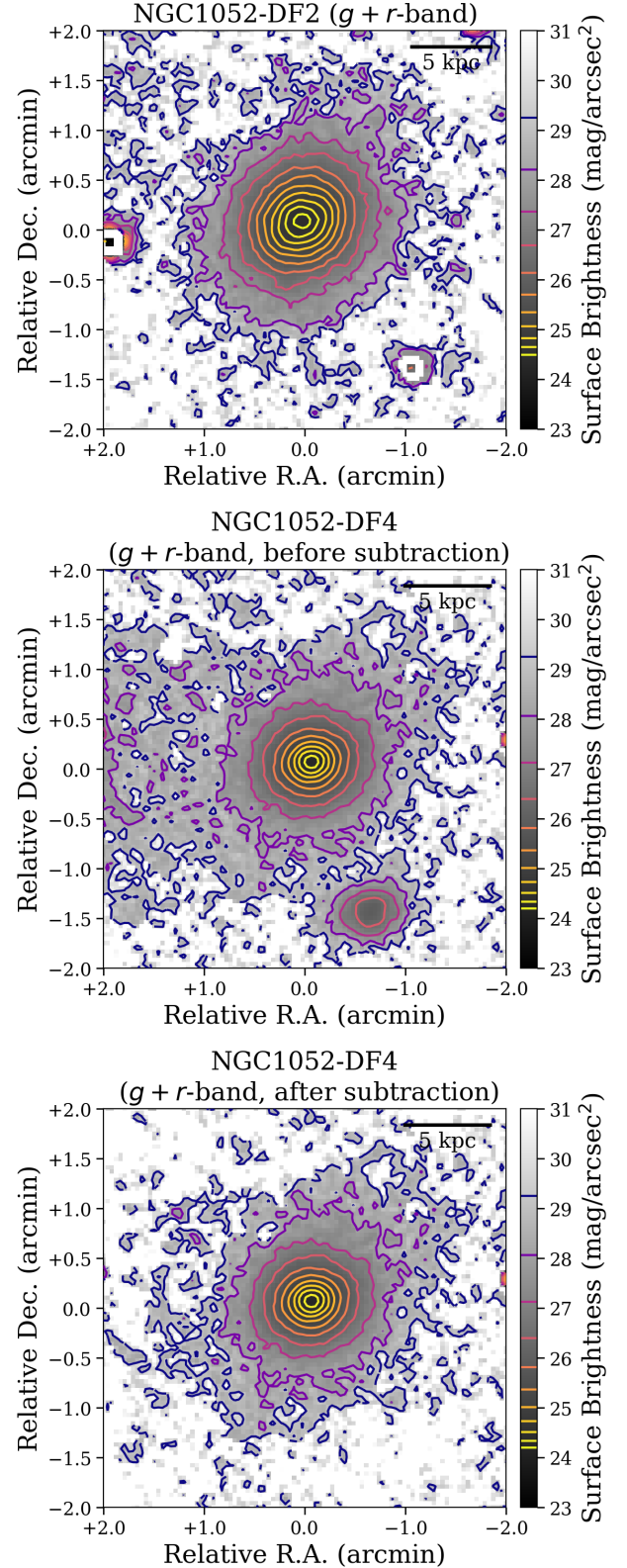


Figure 4. Low surface brightness maps of NGC1052-DF2 (top panel) and NGC1052-DF4 before (middle panel) and after (bottom panel) subtracting models of NGC1052-DF5 and NGC1035.

³ As detailed in Appendix B of <https://arxiv.org/pdf/1910.12867v1.pdf>, a preprint version of van Dokkum et al. (2020) which included a description of the method that we removed in the final version. We are planning to publish it in a standalone paper (van Dokkum et al. in prep).

⁴ Note that it is more appropriate to quantify the depth of specific regions under study; for Fig. 4, we find a **3σ limit of $\mu_{g+r} = 28.99 \text{ mag arcsec}^{-2}$ on $10''$ scales for DF2** ($\mu_{g+r} = 29.63 \text{ mag arcsec}^{-2}$ using Román et al. 2020) and **$\mu_{g+r} = 28.97 \text{ mag arcsec}^{-2}$ for DF4** ($\mu_{g+r} = 29.36 \text{ mag arcsec}^{-2}$ using Román et al. 2020).

of external tidal features, we first model and subtract NGC1052-DF5 and NGC1035.

To generate our models, we make use of Photutils, Bradley et al. (2020)’s Python implementation of the isophote fitting algorithm of Jedrzejewski (1987). This procedure fits the center, position angle, and ellipticity⁵ of individual ellipses with fixed semimajor axis lengths to image data in order to identify the shape of isophotes of the same length. The procedure is repeated for ellipses with semimajor axes sampled geometrically (spaced by a factor of 1.1 by default, i.e. 10%) between predefined minima and maxima. These were selected based on Dragonfly’s PSF, visual inspection of residual images, and the ability of the algorithm to actually fit morphology, as regions with insufficient signal are modeled in a non-iterative mode (although such ellipses were still sometimes included to ensure reasonable residuals that did not leave behind any emission clearly belonging to the galaxy in question).

In order to simultaneously model the outskirts of NGC1052-DF4, NGC1052-DF5, and NGC1035 we adopt the following approach. First, we generate an initial model of NGC1052-DF4, subtract it from the original image, and fit a model of NGC1052-DF5 to the residual image. This NGC1052-DF5 model is then subtracted from our original image, allowing us to generate an improved model of NGC1052-DF4. We then subtract this improved NGC1052-DF4 model from our original image and fit a model of NGC1035 to the new residual image. After generating and subtracting a new model of NGC1052-DF4 from an image with both neighboring galaxies removed, we fit a final model of NGC1052-DF5. We find that this procedure has converged at this point, with further iterations leading to little model improvement. We show our resulting final models of NGC1052-DF5 and NGC1035 in Appendix B. In Fig. 4, we show the final image of NGC1052-DF4 with both neighboring galaxies removed.

4.2. Morphological Models

The contours of the two galaxies look remarkably similar, with both showing a gradual increase in the ellipticity and a gradual change in the position angle of the isophotes. We do not detect distinct tidal tails, suggesting that we have not directly observed the tidal radius of an ongoing interaction where unbound material is being stripped away. Still, the elongated contours in Fig. 4

may indicate material still bound to the galaxies being actively distorted or relic distortions which arose at pericentric passage.

To quantify these aspects we examine the shape of the two galaxies using the elliptical isophote fitting method described above in Section 4.1. To improve the precision of our morphological model, we further restrict our convergence criteria (so that either the largest harmonic amplitude, representing the imperfection of an elliptical isophote, must be below 1% of the rms or the number of fitting iterations for an individual isophote reaches a maximum of 1,000) and increase the geometric step size to 17.5% for a better signal to fit the galaxies’ outskirts while maintaining sufficient radial coverage. The results are shown in Fig. 5; the fit models and residuals are given in Appendix B. To provide an estimate of the uncertainty for isophote position angle, ellipticity, and surface brightness we inserted our originally fit model into 30 different locations near NGC1052 as listed in Appendix C and re-fit the galaxy in this new environment using the same set of semimajor axis lengths. The shading in Fig. 5 represents the fifth-largest and fifth-smallest instances of each quantity from these 30 fits (i.e., the 68% confidence interval).

As with the contours in Fig. 4, in Fig. 5 we see that both galaxies’ isophotes become elliptical in their outer regions. There is a visually identifiable location where the galaxies begin a roughly linear increase in their ellipticity. Moreover, the isophotes become steadily more twisted as well, with the position angles of the galaxies’ outermost regions significantly rotated compared to their interior. The morphological profiles appear to be similar, though NGC1052-DF4 reaches a higher ellipticity at comparable radii and becomes slightly more twisted compared to its orientation at inner radii. The similarities imply the galaxies are experiencing a similar underlying tidal field, indicating that the galaxies are indeed both being disturbed by NGC1052 and might be at a similar physical 3D distance from that galaxy. There also is a point, again similar for both NGC1052-DF2 and NGC1052-DF4, where the galaxies’ surface brightness profiles deviate from Sérsic fits. We note that the profiles of the two galaxies do differ, with a Sérsic index $n_{\text{DF2}} = 0.64$ for NGC1052-DF2 compared to $n_{\text{DF4}} = 0.85$ for NGC1052-DF4 and an effective (half light) radius $R_{\text{e,DF2}} = 24''.8$ compared to $R_{\text{e,DF4}} = 19''.8$. To mitigate the effect of the PSF, we only included isophotes with radii greater than $5''$, i.e. diameters over twice the FWHM, in our model. We find that adopting the 2D Sérsic model from van Dokkum et al. (2018a, 2019), which accounted for the PSF using

⁵ Note that in this work we refer to ellipticity rather than eccentricity, with the former generally taking on smaller values to represent more elongated ellipses; e.g., an ellipticity of 0.2 corresponds to an eccentricity of 0.6.

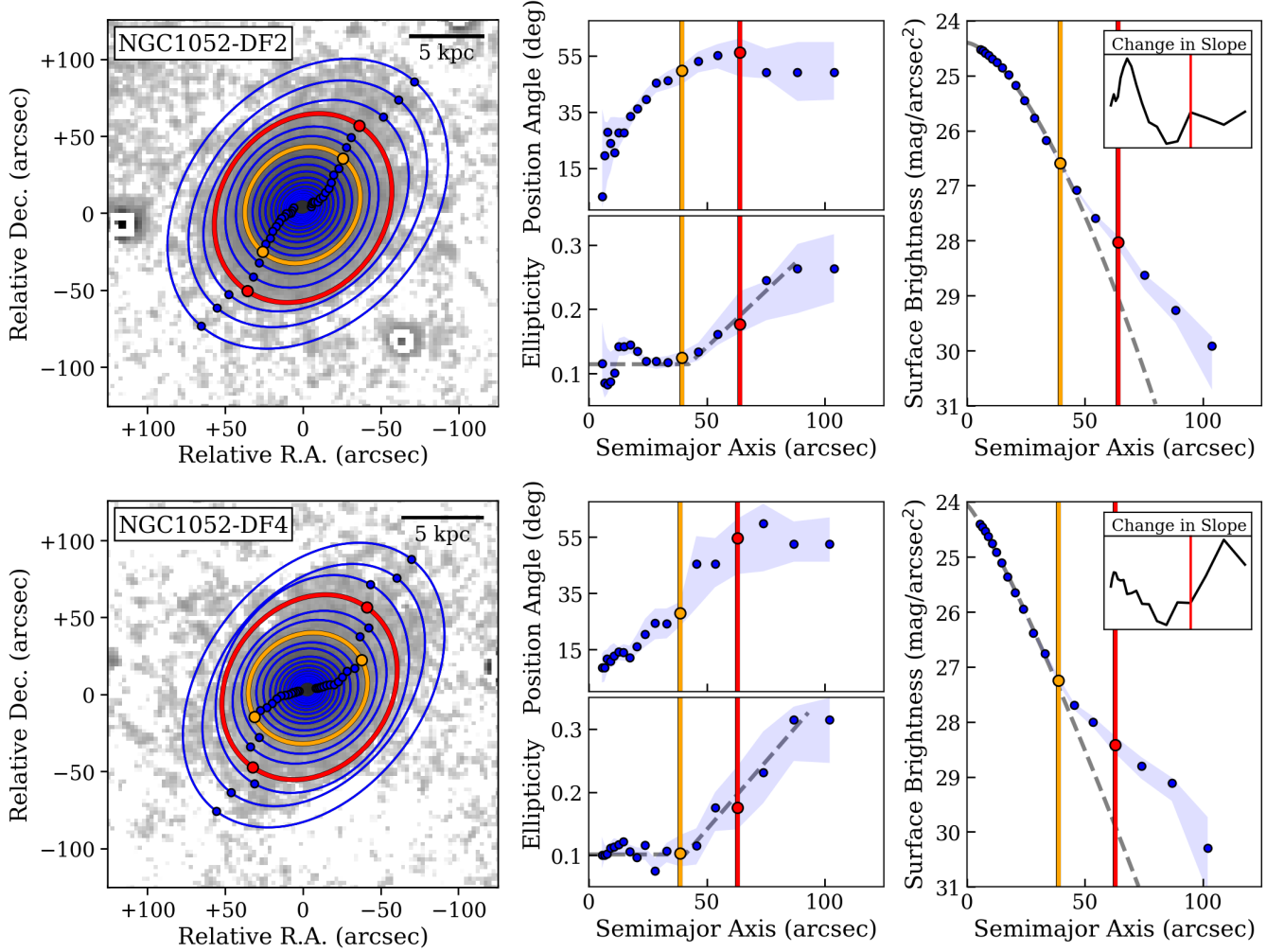


Figure 5. The morphology of NGC1052-DF2 (*top*) and NGC1052-DF4 (*bottom*) as derived from an isophotal analysis. *Left panel:* best-fit elliptical isophotes of equal brightness, with vertices (*circular markers*) given to illustrate trends in the position angle. *Middle panel:* Position angle (*top*) and ellipticity (*bottom*) as a function of the semimajor axis of the fitted isophotes. The onset of distortions is determined through a fit (*grey dashed line*) to Eq. (5), with the isophote nearest to x_0 indicated in all panels (*orange circles and lines*). *Right panel:* The surface brightness of each isophote, along with a Sérsic fit (*grey dashed line*). The tidal break is given as the innermost isophote that exceeds the Sérsic fit by at least $1 \text{ mag arcsec}^{-2}$ and is indicated in all panels (*red circles and lines*). To compare to the definition from Johnston et al. (2002), the change in the slope from isophote to isophote is given in an inset panel. As an estimate of uncertainty, we re-fit our model in 30 different locations, listed in Appendix C, and report the 68% confidence interval of values reached at a given semimajor axis length (*blue shading*). Ellipses with diameters shorter than twice the PSF’s FWHM are not shown and were excluded from our analysis.

GALFIT’s convolution technique (Peng et al. 2002), has little effect on our findings.

To provide a quantitative estimate for the location where tidal distortions arise, we fit the ellipticity profile $\varepsilon(r)$ of the two galaxies with the function

$$\varepsilon(r) = \begin{cases} \varepsilon_0 + a \times (r - r_{\text{distort}}) & \text{if } r > r_{\text{distort}} \\ \varepsilon_0 & \text{if } r \leq r_{\text{distort}} \end{cases} \quad (5)$$

using a horizontal line to account for the undisturbed region and an inclined line to represent the distorted

outskirts, labeling their intersection r_{distort} .⁶ We exclude the outermost isophote from this fit since it was modeled in the non-iterative mode. The onset of distortions occurs at $\sim 40''$ in both galaxies, corresponding to a physical size of $r_{\text{distort}} = 4 \pm 1 \text{ kpc}$, with the uncertainty reflecting the gap between successive isophotes

⁶ Though we were not able to adopt the exact definition of r_{distort} from Johnston et al. (2002) since both NGC1052-DF2 and NGC1052-DF4 have a finite intrinsic ellipticity, here we followed the author’s suggestion to identify the point where the ellipticity significantly changes.

and distance uncertainties (Danieli et al. 2020; Shen et al. 2021b; note that there is no correction for projection effects, as these are accounted for by Johnston et al. 2002). While this is technically within the detectable limits of previous works, the inflection point in the ellipticity profile was only identifiable due to the increasing $\varepsilon(r)$ beyond r_{distort} . This would have been imperceptible in studies which were not able to detect structure out to $\gtrsim 75''$, such as the initial Dragonfly image used to study NGC1052-DF2 and NGC1052-DF4.

As explained in Section 2, this distortion radius may represent material, either bound or unbound, being disrupted by an ongoing interaction, or a disturbance that occurred at pericentric passage which has not yet relaxed back to an equilibrium state (although this may still be captured by the results of Johnston et al. 2002 unless the orbit is highly elliptical or unbound). Thus, r_{distort} may represent either the lower bound of the instantaneous tidal radius, or the approximate tidal radius at pericenter. In order to extract an upper bound of the instantaneous tidal radius, we must investigate the galaxies' surface brightness profiles.

To quantitatively pinpoint the region where the galaxies' surface brightness profiles have an excess of light, we fit a Sérsic profile to the isophotes' surface brightness (as in Montes et al. 2020) and identify r_{break} as the innermost isophote that exceeds the fit by 1 mag arcsec⁻².⁷ We determine that the break in the galaxies' surface brightness, approximately half of the tidal radius upper bound, occurs at $\sim 65''$ in both galaxies. Given the wide gaps between isophotes at the outskirts, r_{break} may lie in the range 55–75'' and correspond to sizes anywhere from 5–8 kpc (Danieli et al. 2020; Shen et al. 2021b).

4.3. Comparison to *HST* Star Counts

Before moving to an interpretation of our results we test the central finding of significant radial change in the isophotes using star counts in *HST* images. Dragonfly's large PSF, and the necessary subtraction of compact sources using the MRF algorithm, make it difficult to study the galaxies' innermost regions. To circumvent this limitation we utilize the *HST* observations from Shen et al. (2021b) and Danieli et al. (2020), whose depth and high resolution facilitated the identi-

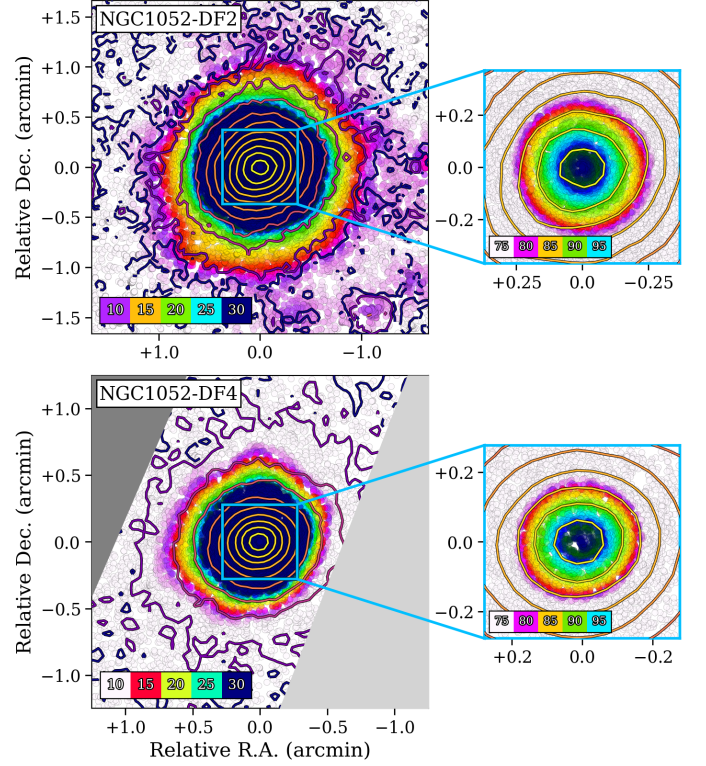


Figure 6. Red giants in NGC1052-DF2 (*top panel*) and NGC1052-DF4 (*bottom panel*) which were individually resolved by deep *HST* observation, colored according to local stellar density. Contours from Fig. 4 are overlaid for comparison to Dragonfly, and zoom-in panels are included to aid in examination of central regions. Color scales are given as percentages of the peak density. Light grey shading indicates regions where star counts were not taken, and dark grey shading indicates the *HST* image boundary. We caution that density estimates near this boundary may be unreliable due to high noise levels.

fication of individual red giants in both NGC1052-DF2 and NGC1052-DF4. This allows us to characterize the morphologies of the galaxies' central regions directly from the distribution of their stars.

In Fig. 6 we plot each galaxies' resolved red giant population, colored according to local stellar density. The stars were identified with DOLPHOT (Dolphin 2000) and filtered to ensure reliable photometry using the quality cuts described by Shen et al. (2021b) and Danieli et al. (2020), with a final total of 19,001 stars in NGC1052-DF2 and 9,287 for NGC1052-DF4 (note that the images were taken over 40 and 12 orbits respectively, with the former achieving a higher depth). Stellar density was determined using a kernel density estimate, summing over Gaussian-convolved stars to find the density at a given point. Applying the same isophote fitting technique we used in modeling Dragonfly data to

⁷ $\Delta\gamma$, the change in slope of the surface density used by Johnston et al. (2002) to define r_{break} , depends on step size so that a direct comparison was not possible and $\Delta\gamma_{\text{lim}} = 0.2$ and 1.0 was not reached for either galaxy. Comparing to the change in slope we do calculate, taking γ as the average of the slope between the central and two neighboring isophotes, we find that this point occurs just outside the minima in $\Delta\gamma$, which indeed was approximately the point which Johnston et al. (2002)'s criteria labels r_{break} .

the density map, we find that both galaxies have a central ellipticity of $\varepsilon \lesssim 0.1$. Thus, we confirm that the innermost regions of both galaxies are indeed relatively spheroidal, as seen in the inner contours of Fig. 4 and the findings of previous works (van Dokkum et al. 2018a, 2019; Müller et al. 2019).

4.4. Distance Implications

As explored in Section 2, low mass satellites are easily disrupted by tidal fields, while high mass satellites must be close to a perturbing galaxy to be tidally stripped. Thus, the identification of tidal features may be used to characterize NGC1052-DF2 and NGC1052-DF4's orbital position and mass. A first item of interest is the distance between the galaxies along the radial direction from earth, i.e. the line-of-sight.

For a fixed dark matter halo mass, there is a maximum distance from NGC1052 along the line-of-sight that would be consistent with the observed tidal distortions.⁸ Since the maximum instantaneous tidal radius from Johnston et al. (2002) is $r_{\text{tid,inst}} = 2 \times r_{\text{break}}$, the maximum absolute distance from NGC1052, R_{max} , is given by

$$R_{\text{max}} = 2 r_{\text{break}} \left(\frac{3 \times M(R_{\text{max}})}{m_*(2 r_{\text{break}}) + m_h(2 r_{\text{break}})} \right)^{1/3} \quad (6)$$

where $m_*(r)$ is the satellite's enclosed stellar mass, $m_h(r)$ is the satellite's enclosed dark matter, and $M(R)$ is NGC1052's mass profile. We find $m_*(r)$ by integrating over each galaxies' Sérsic profile and normalizing to mass estimates of van Dokkum et al. (2018a, 2019). We ignore the galaxies' gaseous content since this has been measured to be negligible compared to the stellar mass (Chowdhury 2019; Sardone et al. 2019, lower by 2–3 orders of magnitude). We take $m_h(r)$ for a given total mass m_{vir} from an NFW profile with a concentration $c = 9.6 \times (m_{\text{vir}}/10^{13} \text{ M}_\odot)^{-0.13} \times (1+z)^{-1}$ (appropriate for satellite galaxies following Bullock & Johnston 2005) and a virial radius $r_{\text{vir}} = (Gm_{\text{vir}}/100H^2(z))^{1/3}$. $M(R)$ is taken from Forbes et al. (2019), an NFW profile with $c = 7.0$, $M_{\text{vir}} = 6.2 \times 10^{12} \text{ M}_\odot$, $R_{\text{vir}} = 390 \text{ kpc}$, and a $4 \times 10^{11} \text{ M}_\odot$ central baryonic component. We allow $M(R)$ to continue increasing beyond R_{vir} to account for other objects within the group contributing to NGC1052's tidal field such as NGC1042 and NGC1047. To solve Eq. (6) and find the maximum line-of-sight distance, we create a radial grid well sampled in log-space

⁸ We may also use r_{distort} to find the minimum possible line-of-sight separation from NGC1052 a satellite could be and exhibit the observed tidal features, although we find this is only relevant in the case that NGC1052-DF2 is almost completely dark matter free. See Section 4.5 for continued discussion.

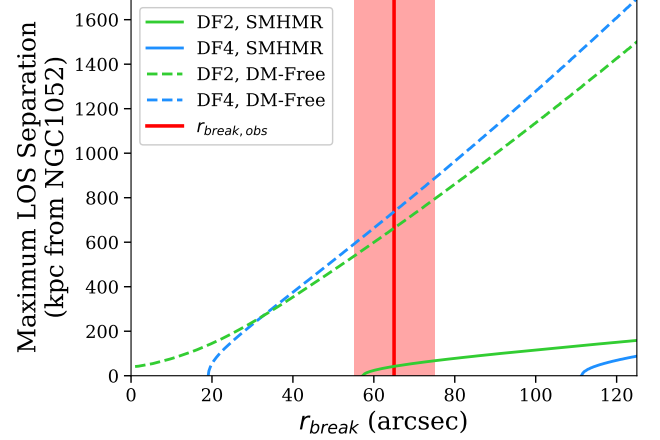


Figure 7. Deriving maximum line-of-sight separations from NGC1052 consistent with our observation. For a range of r_{break} values we infer what the maximum line-of-sight from the satellite (DF2 in green, DF4 in blue) to NGC1052 would be using an integrated Sérsic profile as a stellar mass distribution and either no dark matter (dashed lines) or a dark matter halo with an SMHMR from Behroozi et al. (2013) and the same NFW parameters as in Fig. 1 (solid lines). The observed r_{break} (red solid line) is included with shading to represent the distance between neighboring isophotes (not a formalized error evaluation).

representing a wide range of possible R_{max} values. At each gridpoint, we calculate Eq. (6) from $M(R_i)$, using the satellite's sky position and trigonometric relations to find the corresponding separation along the radial direction from earth, r_{break} 's physical size, $m_*(2 r_{\text{break}})$, and $m_h(2 r_{\text{break}})$. Finally, we identify the gridpoint where R_i is closest to the corresponding R_{max} .

In Fig. 7 we repeat this procedure to find the maximum offset from NGC1052 along the line-of-sight for both an m_{vir} from the stellar mass-halo mass relation (SMHMR, taken from Behroozi et al. 2013) and for a galaxy where the dark matter content is negligible. We find that, if NGC1052-DF4 had a 'normal' dark matter content, it would need to be closer to NGC1052 than it appears in flat sky projection to have the observed r_{break} (or any $r_{\text{break}} \lesssim 110''$ for that matter). This strongly supports the conclusion that NGC1052-DF4 is dark matter deficient. Similarly, NGC1052-DF2 would need to be well within NGC1052's virial radius at a line-of-sight separation of $\lesssim 70 \text{ kpc}$ (a difference caused by NGC1052-DF4's greater sky projected distance). This would imply a small DF2-DF4 line-of-sight separation which is ruled out as it would be in $> 4\sigma$ disagreement with the tip of the red giant branch estimate of Shen et al. (2021b). However, if the galaxies indeed are dark matter deficient, NGC1052-DF2 and NGC1052-DF4 may be offset from NGC1052 by up to

800 and 900 kpc, respectively, which together is within the error bounds of Shen et al. (2021b). The range of halo masses consistent with both Shen et al. (2021b) and our observations is further explored in Section 4.6.

4.5. Pericenter Estimates

In the previous section we assumed that the observed tidal features could be related to the instantaneous tidal radius using the results of numerical simulation by Johnston et al. (2002). Given the limitations discussed in Section 2, in this section we instead explore the assumption that the onset of distortions is approximately the tidal radius at pericentric passage, and that subsequent interaction as well as the dissipation of these features through mechanisms like phase mixing had a negligible effect. In this case, we may use Eq. (1) to provide a range of possible values for the galaxies’ closest approach to NGC1052.

If the orbit is bound, the angular speed at pericenter may be no smaller than $\Omega_{\min} = V_{\text{circ}}/R$ and no greater than $\Omega_{\max} = \sqrt{2}V_{\text{circ}}/R$, since \vec{V} is perpendicular to \vec{R} at pericenter. Given that the galaxies appear to be dark matter deficient, let us make the assumption that the mass enclosed at r_{distort} is approximately the stellar mass alone which can be found from the integrated Sérsic profiles. Using Eq. (1) and Forbes et al. (2019)’s NFW profile, taking into account the $35 - 45''$ range in r_{distort} we find a pericenter of $120 - 190$ kpc for NGC1052-DF2 and $130 - 210$ kpc for NGC1052-DF4. If the galaxies do have significant dark matter content, they may have had closer approaches associated with the tidal features.

Several implications may be drawn from these ranges. First, such 10^2 kpc-scale pericenter estimates are over an order magnitude less than Shen et al. (2021b)’s 2.1 ± 0.5 Mpc DF2-DF4 distance constraint. Thus, if r_{distort} indeed represents r_{tid} at pericentric passage, at least one of the galaxies has traveled great distances of order 10^3 kpc since pericenter and was once much closer to NGC1052 than it is today. Second, taking into account NGC1052-DF2’s lower pericenter bound and its sky projected distance from NGC1052, a separation along the line-of-sight from NGC1052 of $\ll 90$ kpc may challenge the notion that NGC1052-DF2 lacks dark matter. That is, NGC1052-DF2 is not distorted enough to be at $\ll 90$ kpc from NGC1052 along the line-of-sight if it is completely dark matter free, although measuring such a small relative offset would require precision not possible with current methodologies. No such minimum exists for NGC1052-DF4 due to its greater sky projected distance from NGC1052.

4.6. Mass Constraint

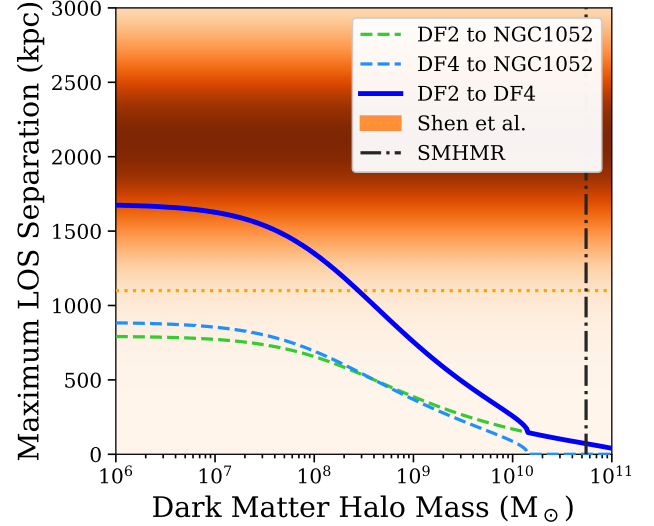


Figure 8. Deriving a dark matter mass upper limit from maximum line-of-sight separations. Assuming a fixed stellar mass profile, for a given dark matter mass we calculate the largest possible line-of-sight distances from NGC1052 to NGC1052-DF2 (green dashed line) and NGC1052-DF4 (light blue dashed line) that would still be consistent with our observed tidal radius. We add these together (dark blue solid line) and compare to Shen et al. (2021b)’s DF2-to-DF4 measurement (orange shading with dotted line at -2σ). We find that if the galaxies have over $3 \times 10^8 M_{\odot}$ in dark matter they are too massive to be as far apart as implied by Shen et al. (2021b) and both show our observed distortions. We emphasize that the x-axis does not include stellar mass, which is left fixed and is dominant at low halo masses.

By combining our observed tidal distortions with Shen et al. (2021b)’s distance constraint, we may obtain an independent constraint on the galaxies’ masses. Shen et al. (2021b) found that – while their absolute distances have a large uncertainty of ≈ 1.5 Mpc – NGC1052-DF2 and NGC1052-DF4 have a well constrained separation of 2.1 ± 0.5 Mpc along the line-of-sight, implying that one or both galaxies is at considerable distance away from NGC1052. However, in Section 4.4 we found that, if the galaxies have a highly massive dark matter halo, they cannot be significantly offset from NGC1052 along the line-of-sight. Considering these facts along with the galaxies’ stellar content, we may draw further implications about their dark matter.

For the halo mass of NGC1052-DF2 and NGC1052-DF4 to be consistent with Shen et al. (2021b), the maximum line-of-sight distances of the two galaxies added together should be above the lower bound of the DF2-DF4 distance constraint. However, if this dark matter halo mass is significantly larger than the true value, then even if the galaxies are on opposite sides of NGC1052, at the maximum distance along the line-of-sight consistent

with our observations, they could not be as far apart as measured by Shen et al. (2021b).

In Fig. 8, we take our observed r_{break} and consider a range of m_{vir} to find which dark matter halo masses are within 2σ agreement with Shen et al. (2021b). We use the same procedure as in Section 4.4, now adjusting m_{vir} of NGC1052-DF2 and NGC1052-DF4, while keeping their stellar mass, r_{break} , and NGC1052’s mass profile fixed. In theory, one could derive separate conditions for both NGC1052-DF2 and NGC1052-DF4 by assuming one had no dark matter and was fixed at either 800 or 900 kpc. However, for the sake of simplicity and realism we assume that they each have approximately the same halo mass and estimate a single constraint for both galaxies. Indeed, we expect this to be the case given their similarities, in particular their stellar masses.

We find that if the galaxies have a dark matter halo above $\sim 3 \times 10^8 M_{\odot}$ (a total mass of $\sim 5 \times 10^8 M_{\odot}$), even if the galaxies are on opposite sides of NGC1052 at their maximum possible distance along the line-of-sight they cannot be as far as measured by Shen et al. (2021b) within 2σ . This mass upper limit is consistent with constraints from kinetic tracers (van Dokkum et al. 2018a; Wasserman et al. 2018; van Dokkum et al. 2019; Danieli et al. 2019; Emsellem et al. 2019). Taking our results at face value and ignoring systematic errors, the galaxies are only consistent with Shen et al. (2021b) if they are not just dark matter deficient (compared to the SMHMR) but nearly dark matter free.

5. DISCUSSION

5.1. Formation Scenario

A key question remains regarding how NGC1052-DF2 and NGC1052-DF4 came to lack dark matter and host such luminous globular clusters. Unfortunately, we cannot well constrain their formation scenario from studying tidal features alone. Though tidal stripping has been proposed as an explanation for NGC1052-DF2 and NGC1052-DF4’s missing dark matter (Ogiya 2018; Macciò et al. 2021; Jackson et al. 2021; Ogiya et al. 2021), the observation of tidal distortions is expected purely based on the galaxies’ dark matter deficiency, independent of whether such tidal interactions originally caused their lack of dark matter. Moreover, while stripping via the tidal field of the same perturber, NGC1052, is able to explain how two objects could both be nearly dark matter free, a complete description of the galaxies’ formation should also include the origin of the galaxies’ bright globular clusters.

Efforts to explain both unusual properties include Shin et al. (2020)’s study of the dark matter deficient remnants of high velocity collisions, with extreme pres-

sure inducing the formation of bright globular clusters as further explored by Lee et al. (2021), as well as Trujillo-Gomez et al. (2020)’s merger hypothesis and Trujillo-Gomez et al. (2021)’s exploration of globular cluster feedback as an explanation for dark matter deficiency. Indeed, the galaxies may have arisen from pure baryonic material, either fragmented on infall (Mandelker et al. 2018) or flung out by quasar winds (Natarajan et al. 1998) or a galaxy merger as in Shin et al. (2020). An important point of our study is that we expect to observe tidal distortions in all such scenarios, unless the galaxies are highly isolated.

Even so, the similarity between the outer regions of NGC1052-DF2 and NGC1052-DF4 does provide new information to help understand the galaxies’ formation process. These galaxies were already known to have similar kinematics, globular cluster populations, stellar masses, sizes, surface brightnesses, and stellar populations; now we add tidal distortions to this remarkable list. Qualitatively, this similarity suggests that the two galaxies have experienced (and are experiencing) a similar tidal field, which in turn implies that they likely are roughly equidistant from the giant elliptical galaxy NGC1052.

5.2. Comparison to Previous Works

Three recent works have undertaken similar efforts to investigate the NGC1052 field for evidence of tidal features (Müller et al. 2019; Montes et al. 2020, 2021). Our observational results largely agree with these previous studies, though in some cases our interpretation of these results differ.

Müller et al. (2019)’s examination of the NGC1052 field in their Fig. 1 is similar to our own Fig. 2, and we confirm the tidal features to the south-east and south-west of NGC1052, as well as the features connecting NGC1047 and NGC1052. Like Müller et al. (2019), we do not observe external streams, tails, or bridges associated with either NGC1052-DF2 or NGC1052-DF4. Our NGC1052-DF2 initial image and generated model also appear similar to their Fig. 3. However, our NGC1052-DF4 results differ in that the outskirts are significantly more elliptical.

Our analysis of NGC1052-DF4 is in better agreement with the results of Montes et al. (2020), who generate a morphological model that is quite similar to our own. Our outermost isophotes have slightly lower surface brightness, which likely has to do with our subtraction of NGC1052-DF5, but are otherwise in agreement. However, a significant difference between our image and that of Montes et al. (2020) is the presence of increased flux to the south-east and north-west which they iden-

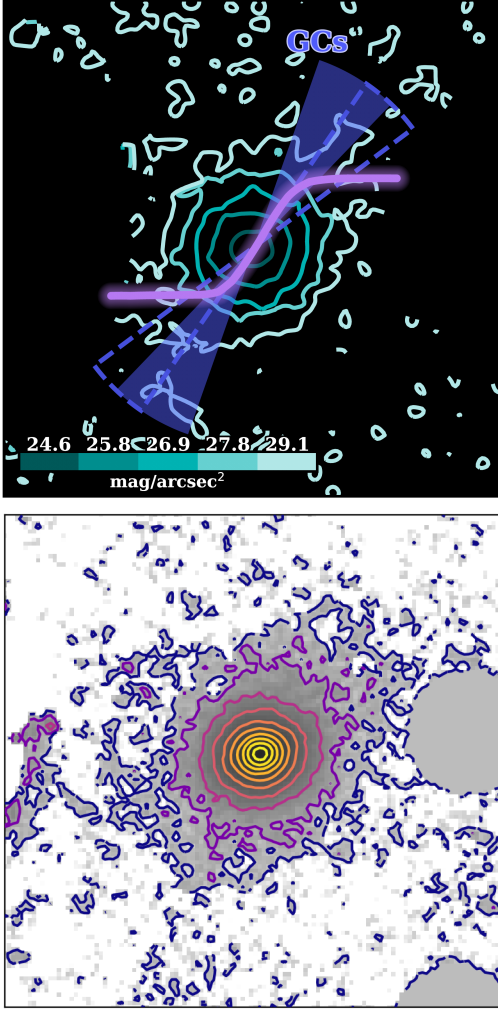


Figure 9. A comparison between the S-shape observed by Montes et al. (2020) (*reproduced in top panel*) and our own image of NGC1052-DF4 (*bottom panel*).

tify as S-shaped tidal tails and evidence of an ongoing interaction with the galaxy NGC1035 (see Fig. 9 for a direct comparison to our own work). This is apparent in their raw data, and persists after subtracting a model for the light of NGC1035. While we observe a significant excess of light in the direction of NGC1035 prior to subtracting a NGC1035 model (due to its overlap with NGC1052-DF2 in projection), we do not observe this excess after removing NGC1035, and we do not find evidence for tidal tails in either case.

Finally, Montes et al. (2021) find that NGC1052-DF2 has no radial variation in its ellipticity or position angle and suggest that this – and an exponential surface brightness profile – implies the presence of a low-inclination disk. With respect to the NGC1052-DF2’s ellipticity, the difference between our work and theirs appears not be in the outskirts of the galaxy, where both

works find $\varepsilon \gtrsim 0.2$, but in the interior of the galaxy where Montes et al. (2021) estimates an ellipticity of $\varepsilon \sim 0.5$; a structure they identify as ‘bulge-like.’ We find a much lower ellipticity in the central regions down to $5''$, and confirm this result with star counts in the deep *HST* image of NGC1052-DF2 (see Fig. 6). This difference may be due to the difficulty of fitting the morphology of a region with a relatively constant surface brightness. With respect to NGC1052-DF2’s surface brightness profile, our fit model is nearly identical to that of Montes et al. (2021). The difference lies in the interpretation, where we fit a Sérsic model rather than a disk and attribute excess light in the outer parts to tidal distortions.

Our interpretation of both galaxies’ profiles is similar to that of Montes et al. (2020) for NGC1052-DF4, namely tidal distortions. Montes et al. (2020, 2021) propose that the similarities between NGC1052-DF2 and NGC1052-DF4 are coincidental and have two independent causes: a face-on massive disk for NGC1052-DF2 and a tidal interaction⁹ for NGC1052-DF4 which stripped its dark matter. In our interpretation, the similarity between the outskirts of NGC1052-DF2 and NGC1052-DF4 has a common cause: tidal effects from NGC1052, which are strong because of the low masses of the galaxies.

5.3. Limitations and Future Efforts

The discovery of tidal features suggests NGC1052-DF2 and NGC1052-DF4 are indeed dark matter deficient. However, the accuracy of our inferred mass and distance limits are hampered by systematic uncertainties inherent to tidal theory. A more appropriate method to derive robust constraints from the observed distortions would be through improved numerical simulation, exploring the region of parameter space consistent with observations of the NGC1052 system in order to constrain the range of NGC1052-DF2 and NGC1052-DF4 masses across all possible orbits.

Within the analytical picture presented, a significant obstacle has been the relation between observed distortions and the true tidal radius where material is unbound. If the tidal radius is indeed within the galaxies’ stellar profile, deeper observation may reveal tidal streams of unbound stars being stripped by NGC1052, thereby providing a more robust upper limit on the tidal radius. Alternatively, if such streams are extremely faint

⁹ With NGC1035, not NGC1052, though we note the best estimates available place NGC1035 at 15.6 ± 2.2 Mpc, NGC1052 at 20.2 ± 1.2 Mpc, and NGC1052-DF4 at 20.0 ± 1.6 Mpc (Kourkchi & Tully 2017; Blakeslee et al. 2001; Danieli et al. 2020).

it may be possible to map stripped material through associated globular clusters. However, our results imply that this radius could be over $2'$ from the galaxies' centers. Thus, it is uncertain whether such tidal tails exist, and with sufficient baryonic content, to be observed.

The next clear observational step to further our work would be an improved NGC1052 distance constraint. Just as Shen et al. (2021b) was able to cancel out systematics in the DF2-DF4 distance estimate, a similar measurement could be obtained for NGC1052 to achieve <1 Mpc uncertainty. This would allow us to test whether or not the two galaxies are indeed at similar distances from NGC1052.

6. SUMMARY AND CONCLUSIONS

In this work we found evidence for tidal distortions associated with NGC1052-DF2 and NGC1052-DF4, two galaxies that had been found to lack dark matter based on their kinematics. Both galaxies show strong position angle twists and become elongated in their outskirts, as is visually apparent in Fig. 4 and quantified by an isophotal analysis in Fig. 5. This is an important result in itself, since we expect such low mass objects to be easily tidally disrupted; unless the galaxies are several hundred kiloparsecs away from any other massive galaxy, they should not remain spheroidal in their outskirts if they are truly dark matter deficient. This is true no matter how the galaxies came to initially lose their dark matter.

Using the results of Johnston et al. (2002) we related these distortions to the tidal radius and derived the maximum separation the galaxies could be from the massive elliptical NGC1052 along the line-of-sight and still show the observed disturbances. We found that, if NGC1052-DF4 had a 'normal' amount of dark matter, its sky-projected distance from NGC1052 is too great to be consistent with our results. Similarly, NGC1052-DF2's radial distance would need to be within 70 kpc of NGC1052's to be consistent with its expected halo mass. However, the galaxies could each be up to nearly 1 Mpc from NGC1052, if they are truly dark matter deficient. We compared these distances together with Shen et al. (2021b)'s 2.1 ± 0.5 Mpc DF2-DF4 measurement to arrive at an upper limit on the galaxies' dark matter content of $\approx 3 \times 10^8 M_\odot$ (a total mass of $\approx 5 \times 10^8 M_\odot$).

This limit is completely independent of previous kinematic constraints, and our findings provide strong, independent evidence that NGC1052-DF2 and NGC1052-DF4 are dark matter deficient. Looking forward, future numerical studies and improved distance measurements may infer more robust mass and orbit constraints from our observations. Such constraints may better inform

efforts to understand how these galaxies came to be, and what they imply for our understanding of galaxy formation and the nature of dark matter.

ACKNOWLEDGMENTS

We thank Frank van den Bosch for highly useful conversations exploring the limits of tidal analysis and for his idea to use our results to constrain the distance of pericentric passage. S. Danieli is supported by NASA through Hubble Fellowship grant #HST-HF2-51454.001-A awarded by the Space Telescope Science Institute, which is operated by the Association of Universities for Research in Astronomy, Incorporated, under NASA contract NAS5-26555. The authors thank the excellent and dedicated staff at the New Mexico Skies Observatory. Support from NSF grants AST1312376 and AST1613582, NSERC, and the Dunlap Institute (funded by the David Dunlap Family) is gratefully acknowledged.

The Legacy Surveys consist of three individual and complementary projects: the Dark Energy Camera Legacy Survey (DECaLS; Proposal ID #2014B-0404; PIs: David Schlegel and Arjun Dey), the Beijing-Arizona Sky Survey (BASS; NOAO Prop. ID #2015A-0801; PIs: Zhou Xu and Xiaohui Fan), and the Mayall z-band Legacy Survey (MzLS; Prop. ID #2016A-0453; PI: Arjun Dey). DECaLS, BASS and MzLS together include data obtained, respectively, at the Blanco telescope, Cerro Tololo Inter-American Observatory, NSF's NOIRLab; the Bok telescope, Steward Observatory, University of Arizona; and the Mayall telescope, Kitt Peak National Observatory, NOIRLab. The Legacy Surveys project is honored to be permitted to conduct astronomical research on Iolkam Du'ag (Kitt Peak), a mountain with particular significance to the Tohono O'odham Nation.

NOIRLab is operated by the Association of Universities for Research in Astronomy (AURA) under a cooperative agreement with the National Science Foundation.

This project used data obtained with the Dark Energy Camera (DECam), which was constructed by the Dark Energy Survey (DES) collaboration. Funding for the DES Projects has been provided by the U.S. Department of Energy, the U.S. National Science Foundation, the Ministry of Science and Education of Spain, the Science and Technology Facilities Council of the United Kingdom, the Higher Education Funding Council for England, the National Center for Supercomputing Applications at the University of Illinois at Urbana-Champaign, the Kavli Institute of Cosmological Physics at the University of Chicago, Center for Cosmology and Astro-Particle Physics at the Ohio State Univer-

sity, the Mitchell Institute for Fundamental Physics and Astronomy at Texas A&M University, Financiadora de Estudos e Projetos, Fundacao Carlos Chagas Filho de Amparo, Financiadora de Estudos e Projetos, Fundacao Carlos Chagas Filho de Amparo a Pesquisa do Estado do Rio de Janeiro, Conselho Nacional de Desenvolvimento Cientifico e Tecnologico and the Ministerio da Ciencia, Tecnologia e Inovacao, the Deutsche Forschungsgemeinschaft and the Collaborating Institutions in the Dark Energy Survey. The Collaborating Institutions are Argonne National Laboratory, the University of California at Santa Cruz, the University of Cambridge, Centro de Investigaciones Energeticas, Medioambientales y Tecnologicas-Madrid, the University of Chicago, University College London, the DES-Brazil Consortium, the University of Edinburgh, the Eidgenossische Technische Hochschule (ETH) Zurich, Fermi National Accelerator Laboratory, the University of Illinois at Urbana-Champaign, the Institut de Ciencies de l’Espai (IEEC/CSIC), the Institut de Fisica d’Altes Energies, Lawrence Berkeley National Laboratory, the Ludwig Maximilians Universitat Munchen and the associated Excellence Cluster Universe, the University of Michigan, NSF’s NOIRLab, the University of Nottingham, the Ohio State University, the University of Pennsylvania, the University of Portsmouth, SLAC National Accelerator Laboratory, Stanford University, the University of Sussex, and Texas A&M University.

BASS is a key project of the Telescope Access Program (TAP), which has been funded by the National Astronomical Observatories of China, the Chi-

nese Academy of Sciences (the Strategic Priority Research Program “The Emergence of Cosmological Structures” Grant #XDB09000000), and the Special Fund for Astronomy from the Ministry of Finance. The BASS is also supported by the External Cooperation Program of Chinese Academy of Sciences (Grant #114A11KYSB20160057), and Chinese National Natural Science Foundation (Grant #11433005).

The Legacy Survey team makes use of data products from the Near-Earth Object Wide-field Infrared Survey Explorer (NEOWISE), which is a project of the Jet Propulsion Laboratory/California Institute of Technology. NEOWISE is funded by the National Aeronautics and Space Administration.

The Legacy Surveys imaging of the DESI footprint is supported by the Director, Office of Science, Office of High Energy Physics of the U.S. Department of Energy under Contract No. DE-AC02-05CH1123, by the National Energy Research Scientific Computing Center, a DOE Office of Science User Facility under the same contract; and by the U.S. National Science Foundation, Division of Astronomical Sciences under Contract No. AST-0950945 to NOAO.

Facilities: Dragonfly, HST (ACS), and DECam (DECaLS).

Software: MRF (van Dokkum et al. 2020), Astropy (Astropy Collaboration et al. 2013, 2018), Photutils (Bradley et al. 2020), Source Extractor (Bertin & Arnouts 1996), and SEP (Barbary 2016).

APPENDIX

A. LOCAL BACKGROUND CORRECTION

The regions surrounding NGC1052-DF2 and NGC1052-DF4 had a significant amount of excess light originating from neighboring galaxies and bright stars excluded from our high surface brightness model. To better analyze emission from the dark matter deficient galaxies themselves, we therefore made a local correction to each galaxy separately by subtracting the mean flux of pixels in the regions listed in Table 1.

B. ISOPHOTE FITTING

In Sections 4.1 and 4.2 we outline the method we utilized to generate galaxy models. In Fig. 10, we give the final model and residuals generated from the described techniques.

C. ERROR ESTIMATE

In order to estimate the uncertainty of our isophotal analysis, we added our models of NGC1052-DF2 and NGC1052-DF4 to 30 different locations near NGC1052 and repeated our fitting procedure. These locations are listed in Table 2.

Table 1. Background Regions

R.A.	Dec.	Radius
(deg)	(deg)	(arcsec)
NGC1052-DF2		
40.47333	-8.42436	20.3
40.43832	-8.36521	17.8
40.41294	-8.39201	17.8
NGC1052-DF4		
39.82145	-8.14999	21.4
39.78004	-8.12458	21.0
39.78511	-8.07410	27.2

Table 2. Locations of Repeated Fitting for Error Analysis

R.A.	Dec.	R.A.	Dec.	R.A.	Dec.
(deg)	(deg)	(deg)	(deg)	(deg)	(deg)
39.8162006	-7.3358901	40.1860284	-7.5700095	40.3688542	-8.5515120
39.8321589	-7.9515584	40.2025026	-8.5785179	40.4626738	-7.4066194
39.8716085	-7.6782209	40.2078246	-8.8191706	40.5392747	-8.2695813
39.8834997	-8.5543915	40.2103322	-8.6098382	40.5418874	-8.7182538
40.0147628	-7.6744495	40.2560314	-7.6300094	40.5471793	-8.7628797
40.0163777	-8.6526040	40.3130732	-8.9059635	40.6362913	-8.7345189
40.0825248	-8.2766276	40.3205831	-7.7666937	40.6526426	-8.4704841
40.0885769	-8.3006303	40.3242276	-7.6040095	40.6543169	-8.1134915
40.1314397	-7.9069662	40.3674423	-8.0746604	40.6642989	-8.9257553
40.1675125	-7.7875162	40.3688038	-7.5520090	40.6851804	-8.9555278

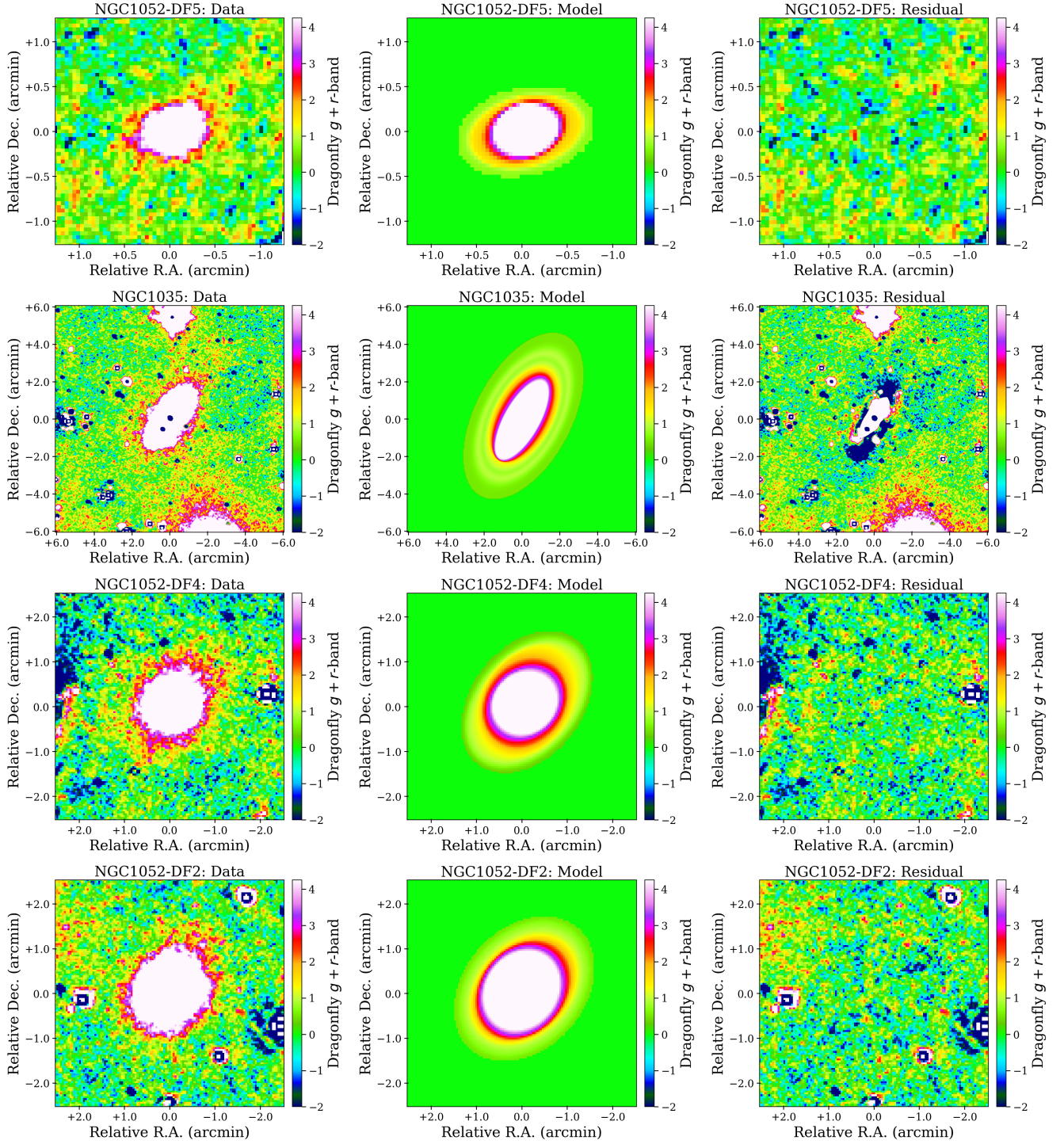


Figure 10. Dragonfly data (*left panels*), fit models (*middle panels*), and fitting residuals (*right panels*) for NGC1052-DF5 (*first row*), NGC1035 (*second row*), NGC1052-DF4 (*third row*), and NGC1052-DF2 (*fourth row*). The colorbar is scaled for optimal analysis of the galaxies' outskirts and the residual images.

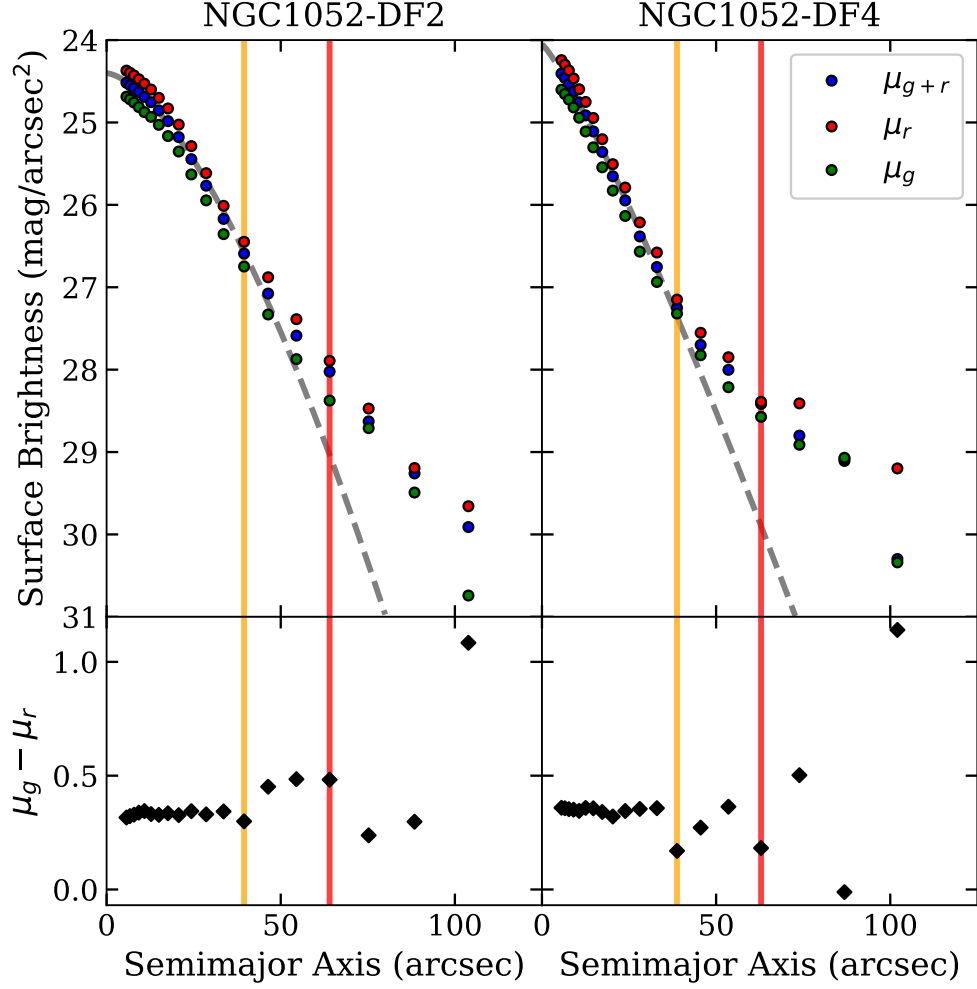


Figure 11. Surface brightness profiles in the g and r bands (*top*) and color profiles (*bottom*) for NGC1052-DF2 (*left*) and NGC1052-DF4 (*right*). 1D Sérsic fits, r_{distort} , and r_{break} from Fig. 5 are indicated by dashed lines.

D. PHOTOMETRIC DATA

This work largely focused on data averaged over the g and r photometric bands. For the use of interested readers, in Fig. 11 we give the surface brightness profiles in each band as well as the $g - r$ color profile. These were computed using the same isophote fitting technique as described in the main text.

REFERENCES

- Abraham, R. G., & van Dokkum, P. G. 2014, *PASP*, 126, 55, doi: [10.1086/674875](https://doi.org/10.1086/674875)
- Astropy Collaboration, Robitaille, T. P., Tollerud, E. J., et al. 2013, *A&A*, 558, A33, doi: [10.1051/0004-6361/201322068](https://doi.org/10.1051/0004-6361/201322068)
- Astropy Collaboration, Price-Whelan, A. M., Sipőcz, B. M., et al. 2018, *AJ*, 156, 123, doi: [10.3847/1538-3881/aabc4f](https://doi.org/10.3847/1538-3881/aabc4f)
- Barbary, K. 2016, *The Journal of Open Source Software*, 1, 58, doi: [10.21105/joss.00058](https://doi.org/10.21105/joss.00058)
- Battaglia, G., Irwin, M., Tolstoy, E., de Boer, T., & Mateo, M. 2012, *ApJL*, 761, L31, doi: [10.1088/2041-8205/761/2/L31](https://doi.org/10.1088/2041-8205/761/2/L31)
- Behroozi, P. S., Wechsler, R. H., & Conroy, C. 2013, *ApJ*, 770, 57, doi: [10.1088/0004-637X/770/1/57](https://doi.org/10.1088/0004-637X/770/1/57)
- Benavides, J. A., Sales, L. V., Abadi, M. G., et al. 2021, *Nature Astronomy*, doi: [10.1038/s41550-021-01458-1](https://doi.org/10.1038/s41550-021-01458-1)
- Bertin, E., & Arnouts, S. 1996, *A&AS*, 117, 393, doi: [10.1051/aas:1996164](https://doi.org/10.1051/aas:1996164)

- Binney, J., & Tremaine, S. 2008, *Galactic Dynamics: Second Edition* (Princeton University Press)
- Blakeslee, J. P., Lucey, J. R., Barris, B. J., Hudson, M. J., & Tonry, J. L. 2001, *MNRAS*, 327, 1004, doi: [10.1046/j.1365-8711.2001.04800.x](https://doi.org/10.1046/j.1365-8711.2001.04800.x)
- Bradley, L., Sipőcz, B., Robitaille, T., et al. 2020, *astropy/photutils*: 1.0.0, 1.0.0, Zenodo, doi: [10.5281/zenodo.4044744](https://doi.org/10.5281/zenodo.4044744)
- Bullock, J. S., & Johnston, K. V. 2005, *ApJ*, 635, 931, doi: [10.1086/497422](https://doi.org/10.1086/497422)
- Choi, P. I., Guhathakurta, P., & Johnston, K. V. 2002, *AJ*, 124, 310, doi: [10.1086/341041](https://doi.org/10.1086/341041)
- Chowdhury, A. 2019, *MNRAS*, 482, L99, doi: [10.1093/mnras/sly192](https://doi.org/10.1093/mnras/sly192)
- Danieli, S., van Dokkum, P., Abraham, R., et al. 2020, *ApJL*, 895, L4, doi: [10.3847/2041-8213/ab8dc4](https://doi.org/10.3847/2041-8213/ab8dc4)
- Danieli, S., van Dokkum, P., Conroy, C., Abraham, R., & Romanowsky, A. J. 2019, *ApJL*, 874, L12, doi: [10.3847/2041-8213/ab0e8c](https://doi.org/10.3847/2041-8213/ab0e8c)
- De Rijcke, S., Prugniel, P., Simien, F., & Dejonghe, H. 2006, *MNRAS*, 369, 1321, doi: [10.1111/j.1365-2966.2006.10377.x](https://doi.org/10.1111/j.1365-2966.2006.10377.x)
- Dey, A., Schlegel, D. J., Lang, D., et al. 2019, *AJ*, 157, 168, doi: [10.3847/1538-3881/ab089d](https://doi.org/10.3847/1538-3881/ab089d)
- Dolphin, A. E. 2000, *PASP*, 112, 1383, doi: [10.1086/316630](https://doi.org/10.1086/316630)
- Emsellem, E., van der Burg, R. F. J., Fensch, J., et al. 2019, *A&A*, 625, A76, doi: [10.1051/0004-6361/201834909](https://doi.org/10.1051/0004-6361/201834909)
- Faber, S. M. 1973, *ApJ*, 179, 423, doi: [10.1086/151881](https://doi.org/10.1086/151881)
- Forbes, D. A., Alabi, A., Brodie, J. P., & Romanowsky, A. J. 2019, *MNRAS*, 489, 3665, doi: [10.1093/mnras/stz2420](https://doi.org/10.1093/mnras/stz2420)
- Jackson, R. A., Kaviraj, S., Martin, G., et al. 2021, *MNRAS*, 502, 1785, doi: [10.1093/mnras/stab093](https://doi.org/10.1093/mnras/stab093)
- Jedrzejewski, R. I. 1987, *MNRAS*, 226, 747, doi: [10.1093/mnras/226.4.747](https://doi.org/10.1093/mnras/226.4.747)
- Johnston, K. V., Choi, P. I., & Guhathakurta, P. 2002, *AJ*, 124, 127, doi: [10.1086/341040](https://doi.org/10.1086/341040)
- King, I. 1962, *AJ*, 67, 471, doi: [10.1086/108756](https://doi.org/10.1086/108756)
- Koch, A., Burkert, A., Rich, R. M., et al. 2012, *ApJL*, 755, L13, doi: [10.1088/2041-8205/755/1/L13](https://doi.org/10.1088/2041-8205/755/1/L13)
- Kourkchi, E., & Tully, R. B. 2017, *ApJ*, 843, 16, doi: [10.3847/1538-4357/aa76db](https://doi.org/10.3847/1538-4357/aa76db)
- Lee, J., Shin, E.-j., & Kim, J.-h. 2021, *ApJL*, 917, L15, doi: [10.3847/2041-8213/ac16e0](https://doi.org/10.3847/2041-8213/ac16e0)
- Lupton, R., Blanton, M. R., Fekete, G., et al. 2004, *PASP*, 116, 133, doi: [10.1086/382245](https://doi.org/10.1086/382245)
- Ma, J., Wang, S., Wang, S., et al. 2020, *MNRAS*, 496, 3741, doi: [10.1093/mnras/staa1775](https://doi.org/10.1093/mnras/staa1775)
- Macciò, A. V., Prats, D. H., Dixon, K. L., et al. 2021, *MNRAS*, 501, 693, doi: [10.1093/mnras/staa3716](https://doi.org/10.1093/mnras/staa3716)
- Mandelker, N., van Dokkum, P. G., Brodie, J. P., van den Bosch, F. C., & Ceverino, D. 2018, *ApJ*, 861, 148, doi: [10.3847/1538-4357/aaca98](https://doi.org/10.3847/1538-4357/aaca98)
- McConnachie, A. W., & Irwin, M. J. 2006, *MNRAS*, 365, 1263, doi: [10.1111/j.1365-2966.2005.09806.x](https://doi.org/10.1111/j.1365-2966.2005.09806.x)
- Mo, H., van den Bosch, F. C., & White, S. 2010, *Galaxy Formation and Evolution* (Cambridge University Press)
- Montes, M., Infante-Sainz, R., Madrigal-Aguado, A., et al. 2020, *ApJ*, 904, 114, doi: [10.3847/1538-4357/abc340](https://doi.org/10.3847/1538-4357/abc340)
- Montes, M., Trujillo, I., Infante-Sainz, R., Monelli, M., & Borlaff, A. S. 2021, arXiv e-prints, arXiv:2106.10283, <https://arxiv.org/abs/2106.10283>
- Mowla, L., van Dokkum, P., Merritt, A., et al. 2017, *ApJ*, 851, 27, doi: [10.3847/1538-4357/aa961b](https://doi.org/10.3847/1538-4357/aa961b)
- Müller, O., Rich, R. M., Román, J., et al. 2019, *A&A*, 624, L6, doi: [10.1051/0004-6361/201935463](https://doi.org/10.1051/0004-6361/201935463)
- Natarajan, P., Sigurdsson, S., & Silk, J. 1998, *MNRAS*, 298, 577, doi: [10.1046/j.1365-8711.1998.01703.x](https://doi.org/10.1046/j.1365-8711.1998.01703.x)
- Navarro, J. F., Frenk, C. S., & White, S. D. M. 1997, *ApJ*, 490, 493, doi: [10.1086/304888](https://doi.org/10.1086/304888)
- Ogiya, G. 2018, *MNRAS*, 480, L106, doi: [10.1093/mnras/sly138](https://doi.org/10.1093/mnras/sly138)
- Ogiya, G., Taylor, J. E., & Hudson, M. J. 2021, *MNRAS*, 503, 1233, doi: [10.1093/mnras/stab361](https://doi.org/10.1093/mnras/stab361)
- Peng, C. Y., Ho, L. C., Impey, C. D., & Rix, H.-W. 2002, *AJ*, 124, 266, doi: [10.1086/340952](https://doi.org/10.1086/340952)
- Planck Collaboration, Aghanim, N., Akrami, Y., et al. 2020, *A&A*, 641, A6, doi: [10.1051/0004-6361/201833910](https://doi.org/10.1051/0004-6361/201833910)
- Read, J. I., Wilkinson, M. I., Evans, N. W., Gilmore, G., & Kleyna, J. T. 2006, *MNRAS*, 366, 429, doi: [10.1111/j.1365-2966.2005.09861.x](https://doi.org/10.1111/j.1365-2966.2005.09861.x)
- Rejkuba, M. 2012, *Ap&SS*, 341, 195, doi: [10.1007/s10509-012-0986-9](https://doi.org/10.1007/s10509-012-0986-9)
- Román, J., Trujillo, I., & Montes, M. 2020, *A&A*, 644, A42, doi: [10.1051/0004-6361/201936111](https://doi.org/10.1051/0004-6361/201936111)
- Sardone, A., Pisano, D. J., Burke-Spolaor, S., Mascoop, J. L., & Pol, N. 2019, *ApJL*, 871, L31, doi: [10.3847/2041-8213/ab0084](https://doi.org/10.3847/2041-8213/ab0084)
- Shen, Z., van Dokkum, P., & Danieli, S. 2021a, *ApJ*, 909, 179, doi: [10.3847/1538-4357/abdd29](https://doi.org/10.3847/1538-4357/abdd29)
- Shen, Z., Danieli, S., van Dokkum, P., et al. 2021b, *ApJL*, 914, L12, doi: [10.3847/2041-8213/ac0335](https://doi.org/10.3847/2041-8213/ac0335)
- Shin, E.-j., Jung, M., Kwon, G., et al. 2020, *ApJ*, 899, 25, doi: [10.3847/1538-4357/aba434](https://doi.org/10.3847/1538-4357/aba434)
- Silk, J. 2019, *MNRAS*, 488, L24, doi: [10.1093/mnras/slz090](https://doi.org/10.1093/mnras/slz090)
- Taylor, J. E., & Babul, A. 2001, *ApJ*, 559, 716, doi: [10.1086/322276](https://doi.org/10.1086/322276)
- Trujillo-Gomez, S., Kruijssen, J. M. D., Keller, B. W., & Reina-Campos, M. 2020, arXiv e-prints, arXiv:2010.05930. <https://arxiv.org/abs/2010.05930>

- Trujillo-Gomez, S., Kruijssen, J. M. D., & Reina-Campos, M. 2021, arXiv e-prints, arXiv:2103.08610.
<https://arxiv.org/abs/2103.08610>
- van den Bosch, F. C., Ogiya, G., Hahn, O., & Burkert, A. 2018, MNRAS, 474, 3043, doi: [10.1093/mnras/stx2956](https://doi.org/10.1093/mnras/stx2956)
- van Dokkum, P., Danieli, S., Abraham, R., Conroy, C., & Romanowsky, A. J. 2019, ApJL, 874, L5, doi: [10.3847/2041-8213/ab0d92](https://doi.org/10.3847/2041-8213/ab0d92)
- van Dokkum, P., Danieli, S., Cohen, Y., et al. 2018a, Nature, 555, 629, doi: [10.1038/nature25767](https://doi.org/10.1038/nature25767)
- van Dokkum, P., Cohen, Y., Danieli, S., et al. 2018b, ApJL, 856, L30, doi: [10.3847/2041-8213/aab60b](https://doi.org/10.3847/2041-8213/aab60b)
- van Dokkum, P., Lokhorst, D., Danieli, S., et al. 2020, PASP, 132, 074503, doi: [10.1088/1538-3873/ab9416](https://doi.org/10.1088/1538-3873/ab9416)
- van Dokkum, P. G., Abraham, R., Merritt, A., et al. 2015, ApJL, 798, L45, doi: [10.1088/2041-8205/798/2/L45](https://doi.org/10.1088/2041-8205/798/2/L45)
- van Dokkum, P. G., & Franx, M. 1995, AJ, 110, 2027, doi: [10.1086/117667](https://doi.org/10.1086/117667)
- Wasserman, A., Romanowsky, A. J., Brodie, J., et al. 2018, ApJL, 863, L15, doi: [10.3847/2041-8213/aad779](https://doi.org/10.3847/2041-8213/aad779)
- Zentner, A. R., & Bullock, J. S. 2003, ApJ, 598, 49, doi: [10.1086/378797](https://doi.org/10.1086/378797)
- Zhang, J. 2018, PhD thesis, University of Toronto, https://jielaizhang.github.io/files/Zhang-Jielai_201811_PhD_Thesis_excludech4.pdf